Measurement of the production of charged pions by protons on a tantalum target

HARP Collaboration

February 1, 2008

Abstract

A measurement of the double-differential cross-section for the production of charged pions in proton–tantalum collisions emitted at large angles from the incoming beam direction is presented. The data were taken in 2002 with the HARP detector in the T9 beam line of the CERN PS. The pions were produced by proton beams in a momentum range from 3 GeV/c to 12 GeV/c hitting a tantalum target with a thickness of 5% of a nuclear interaction length. The angular and momentum range covered by the experiment (100 MeV/$c \leq p < 800$ MeV/c and 0.35 rad $\leq \theta < 2.15$ rad) is of particular importance for the design of a neutrino factory. The produced particles were detected using a small-radius cylindrical time projection chamber (TPC) placed in a solenoidal magnet. Track recognition, momentum determination and particle identification were all performed based on the measurements made with the TPC. An elaborate system of detectors in the beam line ensured the identification of the incident particles. Results are shown for the double-differential cross-sections $\mathrm{d}^2\sigma/\mathrm{d}p\mathrm{d}\theta$ at four incident proton beam momenta (3 GeV/c, 5 GeV/c, 8 GeV/c and 12 GeV/c). In addition, the pion yields within the acceptance of typical neutrino factory designs are shown as a function of beam momentum. The measurement of these yields within a single experiment eliminates most systematic errors in the comparison between rates at different beam momenta and between positive and negative pion production.

HARP collaboration

M.G. Catanesi, E. Radicioni

Università degli Studi e Sezione INFN, Bari, Italy

R. Edgecock, M. Ellis[1], S. Robbins[2,3], F.J.P. Soler[4]

Rutherford Appleton Laboratory, Chilton, Didcot, UK

C. Gößling

Institut für Physik, Universität Dortmund, Germany

S. Bunyatov, A. Krasnoperov, B. Popov[5], V. Serdiouk, V. Tereschenko

Joint Institute for Nuclear Research, JINR Dubna, Russia

E. Di Capua, G. Vidal–Sitjes[6]

Università degli Studi e Sezione INFN, Ferrara, Italy

A. Artamonov[7], P. Arce[8], S. Giani, S. Gilardoni, P. Gorbunov[7,9], A. Grant, A. Grossheim[10], P. Gruber[11], V. Ivanchenko[12], A. Kayis-Topaksu[13], J. Panman, I. Papadopoulos, J. Pasternak, E. Tcherniaev, I. Tsukerman[7], R. Veenhof, C. Wiebusch[14], P. Zucchelli[9,15]

CERN, Geneva, Switzerland

A. Blondel, S. Borghi[16], M. Campanelli, M.C. Morone[17], G. Prior[18], R. Schroeter

Section de Physique, Université de Genève, Switzerland

R. Engel, C. Meurer

Institut für Physik, Forschungszentrum Karlsruhe, Germany

I. Kato[10,19]

University of Kyoto, Japan

U. Gastaldi

Laboratori Nazionali di Legnaro dell' INFN, Legnaro, Italy

G. B. Mills[20]

Los Alamos National Laboratory, Los Alamos, USA

J.S. Graulich[21], G. Grégoire

Institut de Physique Nucléaire, UCL, Louvain-la-Neuve, Belgium

M. Bonesini, A. De Min, F. Ferri, M. Paganoni, F. Paleari

Università degli Studi e Sezione INFN, Milano, Italy

M. Kirsanov

Institute for Nuclear Research, Moscow, Russia

A. Bagulya, V. Grichine, N. Polukhina

P. N. Lebedev Institute of Physics (FIAN), Russian Academy of Sciences, Moscow, Russia

V. Palladino

Università "Federico II" e Sezione INFN, Napoli, Italy

L. Coney[20], D. Schmitz[20]

Columbia University, New York, USA

G. Barr, A. De Santo[22], C. Pattison, K. Zuber[23]

Nuclear and Astrophysics Laboratory, University of Oxford, UK

F. Bobisut, D. Gibin, A. Guglielmi, M. Mezzetto

Università degli Studi e Sezione INFN, Padova, Italy

J. Dumarchez, F. Vannucci

LPNHE, Universités de Paris VI et VII, Paris, France

U. Dore

Università "La Sapienza" e Sezione INFN Roma I, Roma, Italy

D. Orestano, F. Pastore, A. Tonazzo, L. Tortora

Università degli Studi e Sezione INFN Roma III, Roma, Italy

C. Booth, C. Buttar[4], P. Hodgson, L. Howlett

Dept. of Physics, University of Sheffield, UK

M. Bogomilov, M. Chizhov, D. Kolev, R. Tsenov

Faculty of Physics, St. Kliment Ohridski University, Sofia, Bulgaria

S. Piperov, P. Temnikov

Institute for Nuclear Research and Nuclear Energy, Academy of Sciences, Sofia, Bulgaria

M. Apollonio, P. Chimenti, G. Giannini, G. Santin[24]

Università degli Studi e Sezione INFN, Trieste, Italy

J. Burguet–Castell, A. Cervera–Villanueva, J.J. Gómez–Cadenas, J. Martín–Albo, P. Novella, M. Sorel, A. Tornero

Instituto de Física Corpuscular, IFIC, CSIC and Universidad de Valencia, Spain

[1]Now at FNAL, Batavia, Illinois, USA.
[2]Jointly appointed by Nuclear and Astrophysics Laboratory, University of Oxford, UK.
[3]Now at Codian Ltd., Langley, Slough, UK.
[4]Now at University of Glasgow, UK.
[5]Also supported by LPNHE, Paris, France.
[6]Now at Imperial College, University of London, UK.
[7]ITEP, Moscow, Russian Federation.
[8]Permanently at Instituto de Física de Cantabria, Univ. de Cantabria, Santander, Spain.
[9]Now at SpinX Technologies, Geneva, Switzerland.
[10]Now at TRIUMF, Vancouver, Canada.
[11]Now at University of St. Gallen, Switzerland.
[12]On leave of absence from Ecoanalitica, Moscow State University, Moscow, Russia.
[13]Now at Çukurova University, Adana, Turkey.
[14]Now at III Phys. Inst. B, RWTH Aachen, Aachen, Germany.
[15]On leave of absence from INFN, Sezione di Ferrara, Italy.
[16]Now at CERN, Geneva, Switzerland.
[17]Now at Univerity of Rome Tor Vergata, Italy.
[18]Now at Lawrence Berkeley National Laboratory, Berkeley, California, USA.
[19]K2K Collaboration.
[20]MiniBooNE Collaboration.
[21]Now at Section de Physique, Université de Genève, Switzerland, Switzerland.
[22]Now at Royal Holloway, University of London, UK.
[23]Now at University of Sussex, Brighton, UK.
[24]Now at ESA/ESTEC, Noordwijk, The Netherlands.

1 Introduction

The HARP experiment aims at a systematic study of hadron production for beam momenta from 1.5 GeV/c to 15 GeV/c for a large range of target nuclei [1]. The main motivations are the measurement of pion yields for a quantitative design of the proton driver of a future neutrino factory, a substantial improvement of the calculation of the atmospheric neutrino flux [2, 3, 4, 5, 6] and the measurement of particle yields as input for the flux calculation of accelerator neutrino experiments, such as K2K [7, 8], MiniBooNE [9] and SciBooNE [10].

In this paper we address one of the main motivations of the HARP experiment: the measurement of the yields of positive and negative pions for a quantitative design of a proton driver and a target station of a future neutrino factory. In order to achieve the highest number of potentially collected pions of both charge signs per unit of energy a pion production measurement should give the information necessary to optimize both proton beam energy and target material. At the moment the CERN scenario makes provision for a 3 GeV/c – 5 GeV/c proton linac with a target using a high-Z material [11]. Other scenarios are contemplated and may call for higher energy incident beams. In most cases targets are foreseen with high-Z materials. For this reason it was decided to analyse first a series of settings taken with a range of different beam momenta incident on a tantalum target. The different settings have been taken within a short period so that in their comparison detector variations are minimized. Also similar data sets on lead, tin, copper, aluminium, carbon and beryllium have been collected. These will be presented in future papers.

Here, the measurement of the double-differential cross-section, $d^2\sigma^\pi/dpd\theta$ for $\pi^\pm$ production by protons of 3 GeV/c, 5 GeV/c, 8 GeV/c and 12 GeV/c momentum impinging on a thin Ta target of 5% nuclear interaction length (λ_I) is presented.

The HARP experiment [1, 12] makes use of a large-acceptance spectrometer consisting of a forward and large-angle detection system. The forward spectrometer covers polar angles up to 250 mrad which is well matched to the angular range of interest for the measurement of hadron production to calculate the properties of conventional neutrino beams. The HARP publications devoted to the measurements of the π^+ production cross-sections in proton interactions with aluminium [13, 14] and beryllium [15] targets are relevant for the K2K and MiniBooNE neutrino oscillation experiments. The large-angle spectrometer has a large acceptance in the momentum and angular range for the pions relevant to the production of the muons in a neutrino factory. It covers the large majority of the pions accepted in the focusing system of a typical design. The neutrino beam of a neutrino factory originates from the decay of muons which are in turn the decay products of pions produced by a proton beam hitting a production target. For this programme of measurements data were taken with high-Z nuclear targets such as tantalum and lead.

The results reported here are based on data taken in 2002 in the T9 beam of the CERN PS. About one million incoming protons were selected which gave an interaction trigger in the Large Angle spectrometer collected at four distinct beam momenta. After cuts, 150,000 secondary pion tracks reconstructed in the large-angle spectrometer were used in the analysis.

The analysis proceeds by selecting tracks in the Time Projection Chamber (TPC) in events with incident beam protons. Momentum and polar angle measurements and particle identification are based on the measurements of track position and energy deposition in the TPC. An unfolding method is used to correct for experimental resolution, efficiency and acceptance and to obtain the double-differential pion production cross-sections.

The experimental apparatus is outlined in Section 2. Section 3 describes track reconstruction and measurement of dE/dx with the large-angle spectrometer. The event and track selection for the analysis is described in Section 4. The performance of the detector and the methods employed to characterise the performance are shown in Section 5. Section 6 describes details of the cross-section calculation. Results are discussed in Section 7. A comparison with previous data is presented in Section 8. An approximate calculation of the yield of pions within the acceptance of typical focusing systems of some neutrino factory designs is given in Section 9. The conclusions are presented in Section 10. Tables with all cross-section data and a comparison with an alternative analysis of the data are given in appendices.
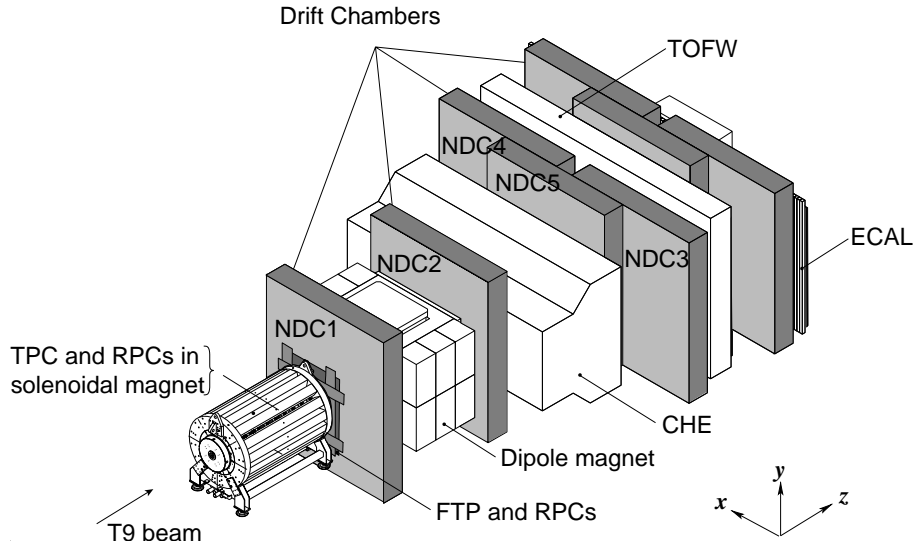
Figure 1: Schematic layout of the HARP detector. The convention for the coordinate system is shown in the lower-right corner. The three most downstream (unlabelled) drift chamber modules are only partly equipped with electronics and are not used for tracking. The detector covers a total length of 13.5 m along the beam direction and has a maximum width of 6.5 m perpendicular to the beam.

2   Experimental apparatus

The HARP detector is shown in Fig. 1. The forward spectrometer is built around a dipole magnet for momentum analysis, with large planar drift chambers (NDC) [16] for particle tracking which had been used originally in the NOMAD experiment [17], and a time-of-flight wall (TOFW) [18], a threshold Cherenkov detector (CHE), and an electromagnetic calorimeter (ECAL) [19] used for particle identification. In the large-angle region a cylindrical TPC with a radius of 408 mm is positioned in a solenoidal magnet with a field of 0.7 T. The TPC is used for tracking, momentum determination and the measurement of the energy deposition dE/dx for particle identification [20]. A set of resistive plate chambers (RPC) form a barrel inside the solenoid around the TPC to measure the time of arrival of the secondary particles [21]. Beam instrumentation provides identification of the incoming particle, the determination of the time when it hits the target, and the impact point and direction of the beam particle on the target. Several trigger detectors are installed to select events with an interaction and to define the normalization.

Data were taken with a number of beam momentum settings and with different target materials and thicknesses. In addition to the data taken with the thin tantalum target of 5% λ_{I}, runs were also taken with an empty target holder, a thin 2% λ_{I} target and a thick 100% λ_{I} target. Data taken with a liquid hydrogen target at 3 GeV/c, 5 GeV/c and 8 GeV/c incident beam momentum together with cosmic-ray data were used to provide an absolute calibration of the efficiency, momentum scale and resolution of the detector. In addition, the tracks produced in runs with Pb, Sn and Cu targets in the same period and with the same beam settings were used for the calibration of the detector, event reconstruction and analysis procedures. The momentum definition of the T9 beam is known with a precision of the order of 1% [22]. The absolute normalization of the number of incident protons was performed using 250,000 'incident-proton' triggers. These are triggers where the same selection on the beam particle was applied but no selection on the interaction was performed. The rate of this trigger was down-scaled by a factor 64. A cross-check of the absolute normalization was provided by counting tracks in the forward spectrometer.

A detailed description of the HARP apparatus is given in Ref. [12]. In this analysis primarily the detector components of the large-angle spectrometer and the beam instrumentation are employed. Below, the detector elements which are important for this analysis will be briefly described.
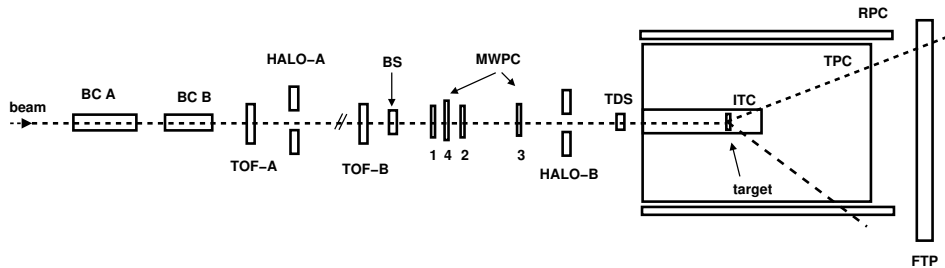
Figure 2: Schematic view of the trigger and beam equipment. The description is given in the text. The beam enters from the left. The MWPCs are numbered: 1, 4, 2, 3 from left to right. On the right, the position of the target inside the inner field cage of the TPC is shown.

2.1 Beam, target and trigger detectors

A sketch of the equipment in the beam line is shown in Fig. 2. A set of four multi-wire proportional chambers (MWPCs) measures the position and direction of the incoming beam particles with an accuracy of $\approx$1 mm in position and $\approx$0.2 mrad in angle per projection. At low momenta the precision of the prediction at the target is limited by multiple scattering and increases to $\approx$1 mrad at 3 GeV/c. A beam time-of-flight system (BTOF) measures the time difference of particles over a 21.4 m path-length. It is made of two identical scintillation hodoscopes, TOFA and TOFB (originally built for the NA52 experiment [23]), which, together with a small target-defining trigger counter (TDS, also used for the trigger and described below), provide particle identification at low energies. This provides separation of pions, kaons and protons up to 5 GeV/c and determines the initial time at the interaction vertex (t_0). The timing resolution of the combined BTOF system is about 70 ps. A system of two N_2-filled Cherenkov detectors (BCA and BCB) is used to tag electrons at low energies and pions at higher energies. The electron and pion tagging efficiency is found to be close to 100%. The fraction of protons compared to all hadrons in the beam is approximately 35%, 43%, 66% and 92% in the 3 GeV/c, 5 GeV/c, 8 GeV/c and 12 GeV/c beam, respectively.

The length of the accelerator spill is 400 ms with a typical intensity of 15 000 beam particles per spill. The average number of events recorded by the data acquisition ranges from 300 to 350 per spill for the four different beam momenta.

The target is placed inside the inner field cage (IFC) of the TPC such that, in addition to particles produced in the forward direction, backward-going tracks can be measured. It has a cylindrical shape with a nominal diameter of 30 mm. The tantalum (99.95% pure) target used for the measurement described here has a nominal thickness of 5% λ_I. Precise measurements of the thickness and diameter have been performed at different locations on its surface. These show a maximum variation of the thickness between 5.55 mm and 5.66 mm and of the diameter between 30.135 mm and 30.15 mm. A set of trigger detectors completes the beam instrumentation: a thin scintillator slab covering the full aperture of the last quadrupole magnet in the beam line to start the trigger logic decision (BS); a small scintillator disk, TDS mentioned above, positioned upstream of the target to ensure that only particles hitting the target cause a trigger; and 'halo' counters (scintillators with a hole to let the beam particles pass) to veto particles too far away from the beam axis. The TDS is designed to have a very high efficiency (measured to be 99.9%). It is located as near as possible to the entrance of the TPC and has a 20 mm diameter, smaller than the target. Its time resolution ($\sim$ 130 ps) is sufficiently good to be used as an additional detector for the BTOF system. A cylindrical detector (inner trigger cylinder, ITC) made of six layers of 1 mm thick scintillating fibres is positioned inside the inner field cage of the TPC and surrounds the target. It provides full coverage of the acceptance of the TPC. The efficiency of the ITC was measured using events which had been taken simultaneously using incident-proton triggers which did not require the ITC and amounts to >99.5%. For the incident-proton triggers, also the interaction trigger bits were stored by the DAQ, although they were not required to record the event. The recorded TPC data in
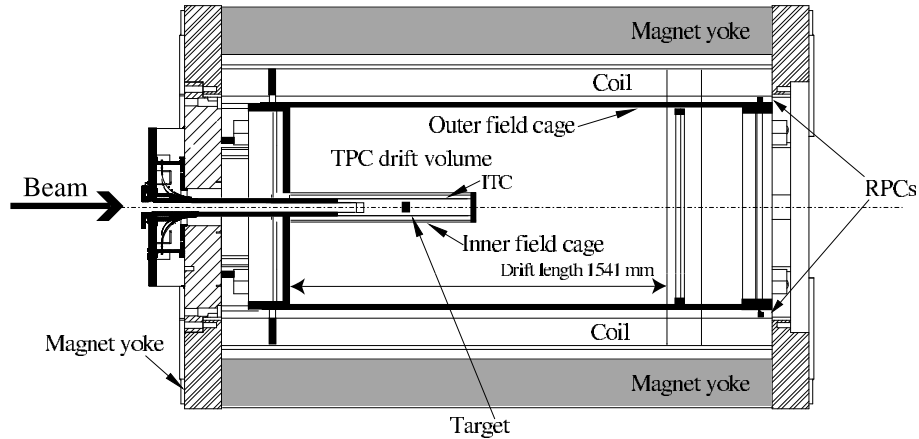
Figure 3: Schematic layout of the TPC. The beam enters from the left. Starting from the outside, first the return yoke of the magnet is seen, closed with an end-cap at the upstream end, and open at the downstream end. The cylindrical coils are drawn inside the yoke. The field cage is positioned inside this magnetic volume. The inner field cage is visible as a short cylinder entering from the left. The ITC trigger counter and the target holder are inserted in the inner field cage. The RPCs (not drawn) are positioned between the outer field cage and the coil.

events taken with the incident proton beam were passed through the track finding algorithm and for each event with at least one TPC track the ITC trigger decision was checked. The efficiency per single ITC layer was found to be typically 80%, giving a large redundancy for the OR-signal to reach the quoted overall efficiency.

2.2   Large-angle spectrometer

The large-angle spectrometer consists of a TPC and a set of RPC detectors inside the solenoidal magnet. The TPC detector was designed to measure and identify tracks in the angular region from 0.25 rad to 2.5 rad from the beam axis. Charged particle identification (PID) can be achieved by measuring the ionization per unit length in the gas (dE/dx) as a function of the total momentum of the particle. Additional PID can be performed through a time-of-flight measurement with the RPCs.

Figure 3 shows the schematic layout of the HARP TPC. The TPC is positioned inside the solenoid magnet. The solenoid provides a magnetic volume with a diameter of 0.9 m, a length of 2.25 m and a field of 0.7 T. Secondary particles enter the forward spectrometer through the downstream end of the return yoke which is left open. At the upstream end there is a small cylindrical hole in the end-cap for the passage of the incident beam and to insert the ITC and target holder inside the IFC. The magnet was previously used for R&D for the TPC of the ALEPH experiment and modified for this experiment. The induced charge from the gas amplification at the anode wires is measured using a plane with twenty concentric rows of pads, each connected to a pre-amplifier. The pad plane is subdivided into six sectors. The anode wires are strung onto six spokes subdividing the six sectors. The pad plane is subdivided radially into 20 rows of pads. The pad dimensions are 6.5 mm × 15 mm and there are from 11 (at the inner radius) to 55 (at the outer radius) such pads per row per sector. The drift volume is 1541 mm long with a field gradient of 111 V/cm, resulting in a maximum drift time of approximately 30 μs. The pad-charges are sampled by an FADC (one per pad) each 100 ns. The total DAQ readout time is 500 μs to 1000 μs per event depending on the event size.

Thirty RPC chambers are arranged in the shape of a barrel around the TPC providing full coverage in azimuth and covering polar angles from 0.3 rad to 2.5 rad with respect to the beam axis. The individual chambers are 10 mm thick, 150 mm wide and 2 m long. Together with the timing measurement of the beam detectors the RPC system provides a measurement of time-of-flight of particles produced at large

angles from the beam axis.

In the present analysis, the TPC provides the measurement for the pattern recognition to find the particle tracks, and to measure their momentum through the curvature of their trajectory. It also provides PID using the measurement of energy deposition. The RPC system is used in this analysis to provide a calibration of the PID capabilities of the TPC.

Besides the usual need for calibration of the detector, a number of hardware shortfalls, discovered mainly after the end of data-taking, had to be overcome to use the TPC data reliably in the analysis. The TPC contains a relatively large number of dead or noisy pads. Noisy pads are disregarded in the analysis and therefore equivalent to dead pads. The problem of dead channels present during operation ($\approx$ 15%) necessitates a day–by–day determination of the dead channel map. The same map is used in the simulation, providing a description of the performance of the TPC adjusted to the conditions of each short period of data taking. A method based on the tracks measured during normal data taking was developed to measure the variations of the overall gain of each pad, including the gas gain, by accumulating for each pad all the data taken during a period in time over which the performance of the chamber can be considered constant (typically a few hours) [12]. In addition, this method allows dead and noisy channels to be identified. It is used to reduce the fluctuation in the response between pads down to a 3% level.

The well-known position of the target and of the end-flange of the IFC are used to determine the drift velocity by reconstructing tracks emerging from these materials. Since the drift velocity varies as a function of operational parameters such as pressure, temperature and gas-mixture, it is determined for each relatively short data taking period. Variations of up to 4% were observed [12]. The precision of the calibration for individual periods is better than 0.5%.

Static distortions of the reconstructed trajectories are observed in the TPC. The most important ones are caused by the inhomogeneity of the magnetic field and an accidental HV mismatch between the inner and outer field cage (powered with two distinct HV supplies). The distortions were studied in detail using cosmic-ray data obtained with a special calibration run performed after the data taking period. Appropriate distortion correction algorithms in the TPC reconstruction software compensate for the voltage offset and for the inhomogeneities of the magnetic field.

Dynamic distortions which are caused by the build-up of ion-charge density in the drift volume during the 400 ms long beam spill are observed in the chamber. Changes in the beam parameters (intensity, steering) cause an increase or decrease in the dynamic distortions. While methods to correct the dynamic distortions are under development, a pragmatic approach is chosen to limit the analysis to the early part of the beam spill where the effects of dynamic distortions are still small. The time interval between spills is large enough to drain all charges in the TPC related to the effect of the beam. The combined effect of the distortions on the kinematic quantities used in the analysis has been studied in detail, and only that part of the data for which the systematic errors can be controlled with physical benchmarks is used. More than 30% of the data can be retained.

The influence of the distortions can be monitored using the average value of the extrapolated minimum distance of secondary tracks from the incoming beam particle trajectory $\langle d'_0 \rangle$. In Fig. 4 this quantity is plotted separately for positively and negatively charged pion tracks and protons as a function of the event number within the spill for the four beam settings used. Due to the sign-convention for d'_0, the distortions shift its value in opposite directions for particles tracks of positive and negative charge. It can clearly be seen that this distance increases with time. The effect also increases with beam momentum; this is expected from the track multiplicity increase. Also the beam intensity was higher for higher beam momenta. As will be shown in the following, data taken under conditions where the average d'_0 is smaller than 5 mm can be analysed reliably. For the analysis presented here, this results in a limit of $\approx$ 100 events per spill, depending on the setting. The performance of the chamber for this subset of the data was studied using several methods, including the analysis of elastic events in exposures of a liquid hydrogen target. These results will be shown in subsequent sections. The small mismatch extrapolated to $N_{\text{evt}} = 0$ visible in the 8 GeV/c and 12 GeV/c data are due to residual static distortions. Although the latter show a variation among different settings a common correction is applied. The systematic error introduced in the momentum calibration by this approximation is estimated to be less than 1%.
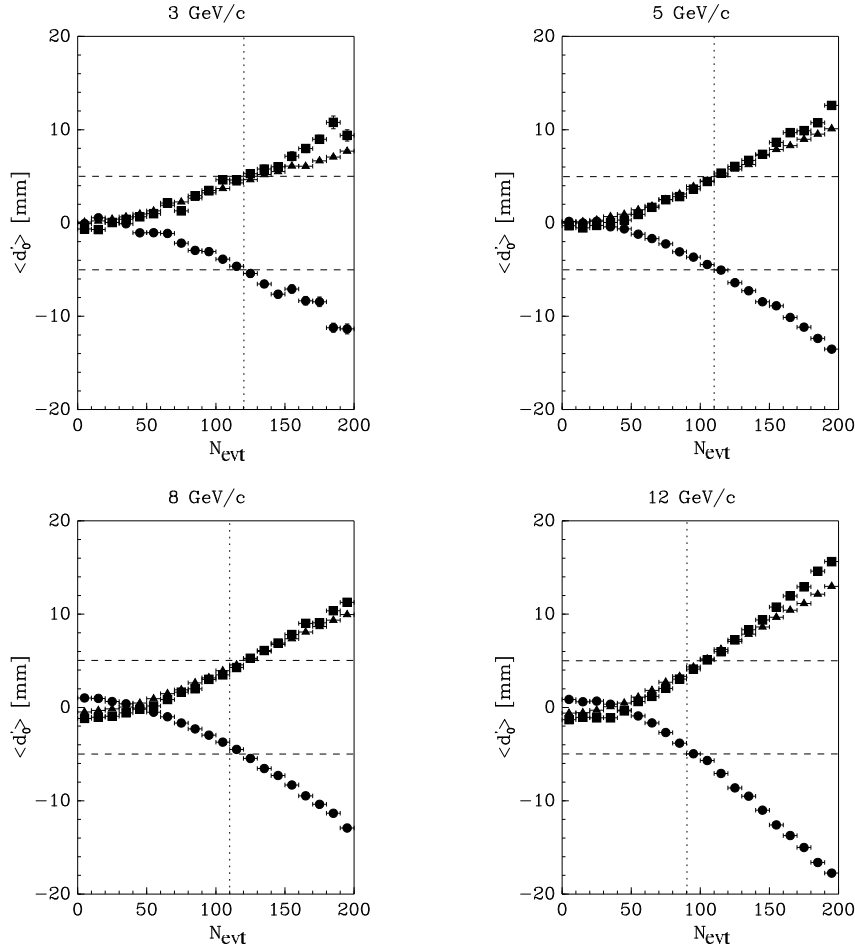
Figure 4: Effect of dynamic distortions as a function of event number in the spill for the four tantalum settings used in the analysis emphasizing the first part of the spill (200 events). The symbols show the average extrapolated distance from the incoming beam particle trajectory for π^- (filled circles), π^+ (filled squares), and protons (filled triangles). The momentum of the beam is indicated in the title of the panels. Data with $\langle d_0' \rangle < 5$ mm have been used in the analysis. The dashed horizontal lines indicate the value at ± 5 mm to guide the eye, while the vertical dotted lines show the maximum value of N_{evt} accepted in the analysis.

3 Track reconstruction

The reconstruction of particle trajectories in the TPC is implemented with a sequence of distinct steps.

After unpacking of the raw data, time-series of flash-ADC values representing the charge collected on pads are combined into clusters on the basis of individual pad rows. Hits in neighbouring pads with time stamps that differ by less than 600 ns are included in the cluster. Each cluster gets a weighted position in the $r\varphi$ direction along the pad row using the pad positions and in the z direction using the time information. The reference time is defined on the rising edge of the signal when the first pulse in a cluster goes over threshold.

The clusters are then assigned to tracks by a general purpose pattern recognition algorithm. This algorithm uses a general framework for track finding in multi-dimensional space [24], in this case applied to a 3-D situation. The framework does not impose a preferred search direction. In an initial phase clusters are sorted into an N-dimensional binary tree to prepare an efficient look-up of nearest neighbours. The algorithm then builds a network of all possible links between the clusters. Links are acceptable if the distance between the clusters is small (accepting hits on nearby pad rows, taking into account possible

gaps in the track hits). Then it builds a tree of connected clusters, starting from 'seeds'. As seed any of the linked pairs of hits is tried, taking first those on the outer pad row and then the unused links on the next inner row, and so on. Despite the magnetic field, the track model approximates tracks locally as straight lines. When from a given link multiple continuations are possible a choice has to be made which continuation is to be used to form the final track. The branch of the tree which is retained as the best continuation of the track is determined by examining pairs of fully grown branches and selecting the better one. Since the tree is built recursively, it suffices to compare possible continuations from a given link pair-wise. The general framework allows the specific implementation to define the criterion used to make this choice. In the case of the trackfinding in the HARP TPC with its low occupancy of hits the choice of the branch with the largest number of clusters is sufficient. Parameters in the framework which can be adjusted to the particular situation are the minimum number of points for an accepted track, the maximum curvature, the maximum distance between consecutive clusters and the criterion to choose the best of two possible solutions for a branch on a tree.

3.1 Momentum measurement

Once clusters are assigned to a track, the track is fitted to a helix. The fitting procedure is based on the algorithm developed by the ALEPH Collaboration [25] with slight modifications, *e.g.* the possibility to fit tracks which spiral for more than 2π [26]. The fit consists of two consecutive steps: a circle-fit in the x–y plane based on a least-square method [27] which defines three parameters, and a subsequent straight line fit in z–s_{xy} plane[1] which defines two other parameters. A helix is uniquely defined by these parameters. The code uses the same sign conventions as in the TASSO and ALEPH software [25] with a particle direction associated to the motion along the helix itself. Different classes of precision can be assigned to clusters along r and ϕ depending on the number of hits that belong to a cluster and depending on whether a cluster is near to a region of dead pads. This classification was developed from studies of the residuals observed in the data and also quantified using simulated data. As was done in the original ALEPH method, weights are applied to take into account the differences in cluster quality, a method which is applicable to errors of systematic nature.

Tracks which are emerging from the target are refitted using the position of the extrapolated beam particle as an extra point in the fit with a weight similar to a TPC hit ('constrained fit'). Refitting the track parameters imposing the vertex constraint improves the momentum resolution significantly at the cost of a moderate loss of efficiency of a few percent. The energy-loss in the materials along the particle trajectory is not taken into account in the fit[2]. However, in the analysis these effects are corrected for (see Section 6.1) by applying the same procedure to the data and the simulation.

A study with the simulation program of the resolution of the inverse of the momentum determination using the constraint of the extrapolated beam particle is shown in Fig. 5. Results for particles emitted at large angles (85^0) are shown together with the behaviour at smaller angles (35^0). The resolution of the measured momentum is compared with the 'true' momentum in the gas. A fit to the distributions with two Gaussians constrained to have the same mean has been performed. The measurement of the RMS of the sum of the Gaussians is compared with the σ of the narrow Gaussian. The RMS is larger by 25%–30% than the σ of the narrow Gaussian, indicating the presence of non-Gaussian tails. The difference between the two angles is expected from the fact that the resolution is a function of p_{T} rather than p. The tails of the distributions are fully taken into account in the analysis. Although the track curvature is measured mainly in the gas, the resolution extrapolates to $p_{\mathrm{T}} = 0$ with a $\approx$2% constant term. This is due to the use of the vertex point as constraint in the fit, which adds the effect of multiple scattering in the inner field cage and trigger counter, and to the use of a perfect helix as track description neglecting inhomogeneities in the magnetic field which are present in the simulation of the trajectories. The experimental measurement of the resolution of the determination of the momentum is consistent with the simulation and will be described in a following section.

Figure 6 shows a simulation study of the resolution of the inverse of the momentum using the constraint of the extrapolated beam particle both with respect to the true momentum in the gas and at the interaction

---

[1]The s_{xy} coordinate is defined as the arc length along the circle in the x-y plane between a point and the impact point.
[2]The constrained fit is performed using the analytical helix track model.
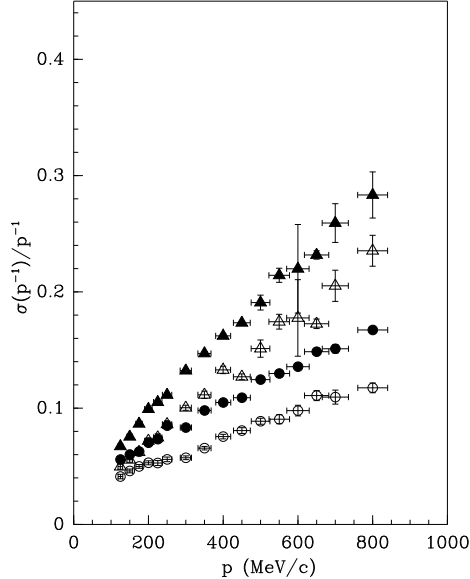
Figure 5: Simulation study of the resolution of the inverse of the momentum determination using the constraint of the extrapolated beam particle. Results for charged pions emitted at large angles (85^0) are shown with triangles, while the circles represent the behaviour at smaller angles (35^0). The resolution of the measured momentum is compared with the 'true' momentum in the gas. All materials in the detector and the target are taken into account in the simulation. A fit with two Gaussians constrained to have the same mean has been performed to the distributions. Filled circles and triangles show the measurement of the RMS of the fitted function, while the open circles and triangles show the σ of the narrow Gaussian.

vertex. The resolution of the momentum determination with respect to the momentum at the interaction vertex suffers from the effect of energy-loss in the material (target, trigger detector, IFC). The large difference of the effect of the material between large and small angles is due to the relatively large transverse dimensions of the tantalum target (15 mm radius) compared to the thickness of only 5.6 mm in the direction of the beam.

3.2   Measurement of dE/dx and time-of-flight

The mean energy-loss per unit length for each particle trajectory is calculated by an algorithm which evaluates the dE/dx for each cluster on the track associated to each curvilinear TPC pad row. The dx is calculated considering the segment of the helicoidal trajectory of the particle in that row, the dE is the total charge collected by the pad plane for that cluster summing all ADC counts collected by the pads that belong to that cluster. The resulting distribution of dE/dx of the individual clusters is expected to follow a Vavilov distribution. To obtain the most reliable estimate for the peak (the most probable value) of the Vavilov distribution, an algorithm has been developed using a truncated mean. The algorithm has been optimized by selecting all clusters of all tracks in slices of momentum for preselected pion and proton samples, respectively; hence this technique allowed a characterization of the dE/dx distributions to be made with extremely high statistics. It is found that calculating an average value using 80% of the clusters, removing the 20% with the highest dE/dx, provides the best estimate of the peak position. In Section 5.5 dE/dx spectra as they are observed in the data are shown.

The particle relativistic velocity β is determined measuring the time-of-flight (TOF) from its production point at the target up to the system of resistive plate chamber (RPC) detectors arranged as a barrel around the TPC. The path-length is determined using the trajectory measured in the TPC. The time of production of the particle is measured using the time the beam particle traverses the BTOF detectors and extrapolating it to the interaction point. The combined time resolution is 180 ps [28]. At present β is not used for PID in the final analysis. However, the PID capabilities with this TOF measurement are
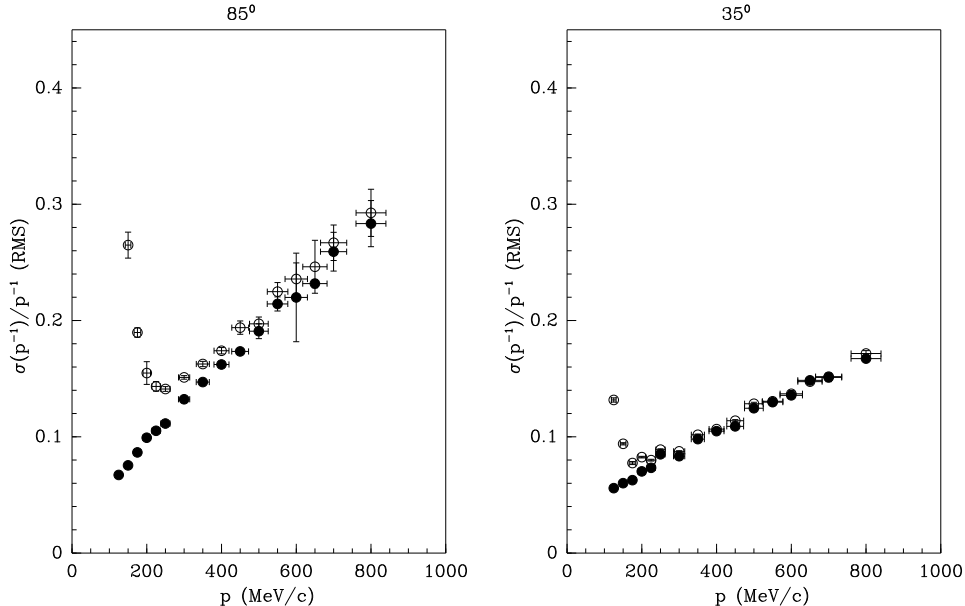
Figure 6: Simulation study of the resolution of the determination of the inverse of the momentum using the constraint of the extrapolated beam particle. The left panel shows the results for charged pions emitted at large angles (85^0), while the right panel shows the behaviour at smaller angles (35^0). All materials in the detector and the target are taken into account. Filled circles show the resolution of the inverse of the momentum determination with respect to the 'true' momentum of the particle in the TPC gas volume for pions (measured by the RMS of the distribution). Open circles and boxes show the resolution with respect to the 'true' momentum at the interaction vertex. The effect of energy-loss in the material (target, trigger detector, IFC) is clearly visible.

used to select pure samples of pions and protons to measure the efficiency and purity of the PID selection using dE/dx.

4   Data selection procedure

The positive-particle beam used for this measurement contains mainly positrons, pions and protons, with small components of kaons and deuterons and heavier ions. Its composition depends on the selected beam momentum. The analysis proceeds by first selecting a beam proton hitting the target, not accompanied by other tracks. Then an event is required to be triggered by the ITC in order to be retained. After the event selection the sample of tracks to be used for analysis is defined. The selection procedure is described below.

The beam time-of-flight system measures time over a distance of 21.4 m which provides particle identification at low energy (up to 5 GeV/c). At 3 GeV/c the time-of-flight measurement allows the selection of pions from protons to be made at more than 5σ, the protons account for about 30% of beam at this momentum. The fraction of protons increases with beam momentum. At higher momenta protons are selected by rejecting particles with a measured signal in either of the beam Cherenkov detectors. The selection of protons for the beam momenta with the Cherenkov detectors has been described in detail in Ref [13]. More details on the beam particle selection can be found in Ref. [12]. Deuterons (and heavier ions) are removed by TOF measurements. A set of MWPCs is used to select events with only one beam particle for which the trajectory extrapolates to the target. An identical beam particle selection was performed for events triggered with the incident-proton trigger in order to provide an absolute normalization of the incoming protons. This trigger selected every 64th beam particle coincidence outside the dead-time of the data acquisition system. The requirement of a trigger in the ITC keeps a sample of one
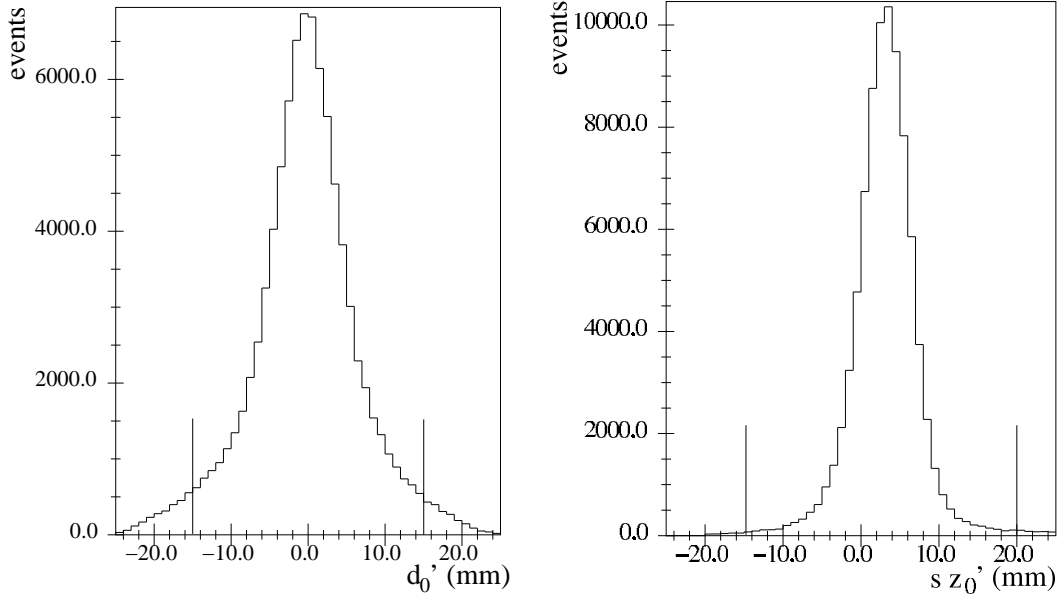
Figure 7: The distribution of d_0' (left panel) and $s\,z_0'$ (right panel) taken with an 8 GeV/c proton beam hitting a tantalum target for tracks with low dE/dx. Cuts (indicated by the vertical bars) are applied at $|d_0'| < 15$ mm and -14.4 mm $< s\,z_0' < 20.0$ mm.

million events for the analysis.

The beam particle has to be accepted by the criteria described above and has to be identified as a proton. In order to avoid large effects of the TPC dynamic distortions only the first N_{evt} events in each spill are retained. Using calibration data sets, the deterioration of the performance of the detector is determined as a function of the strength of the distortions characterized by an average value of d_0' for the same set of events. As a practical solution and to simplify the analysis the 'event number in spill' N_{evt} defines a measure of the time when the event occurred from the start of the spill. This is a good measure of time since the readout time per event is sufficiently constant (about 1 ms/event) and since the beam intensity was so high that the DAQ was running close to saturation. For each setting the N_{evt} criterion was calibrated with the behaviour of the average d_0', $\langle d_0' \rangle$. The part of the spill accepted in the analysis is then defined by determining for each data-taking condition for which value of N_{evt} the average value of d_0' exceeds 5 mm. In practice, the value of N_{evt} is close to 100 in all settings analysed, compared to a typical total number of events per spill of 300.

Cuts are defined to reject tracks from events which arrive randomly in the 30 μs drift time of the TPC secondaries from interactions of other beam particles ('overlays'). In addition, selection criteria are used which preferentially remove tracks from secondary interactions (*i.e.* interactions of the particles produced in the primary interaction). The following selection was applied to retain well-measured particle tracks with known efficiency and resolution.

Tracks are only considered if they contain at least twelve space points out of a maximum of twenty. This cut is applied to ensure a good measurement of the track parameters and of the dE/dx. Furthermore, a quality requirement is applied on the fit to the helix. The latter requirement introduces a very small loss of efficiency.

For tracks satisfying these conditions, a cut is made on d_0', the distance of closest approach to the extrapolated trajectory of the incoming beam particle in the plane perpendicular to the beam direction and z_0', the z-coordinate where the distance of the secondary track and the beam track is minimal. Figure 7 shows the distribution of d_0' and $s\,z_0'$ for the data taken with 8 GeV/c protons on a tantalum target. The variable s is defined as $s = \sin\theta$, where θ is the angle of the particle measured with respect to the nominal beam axis. To avoid the bias due to the change of curvature which occurs for highly ionizing protons traversing the ITC trigger counter and the inner field cage, only outgoing tracks with

Table 1: Total number of events and tracks used in the tantalum 5% λ_I target data sets, and the number of protons on target as calculated from the pre-scaled trigger count.

Data set	3 GeV/c	5 GeV/c	8 GeV/c	12 GeV/c
Total events taken by the DAQ	2291133	2094286	2045628	886305
Protons on target (selected incident-proton×64)	1693376	3251136	6136960	3486016
Accepted protons with interaction triggers	416131	447312	752377	436400
Accepted protons with Large Angle Int. (LAI)	101509	218293	442624	269927
Maximum N_{evt}	120	110	110	90
LAI in accepted part of the spill	38281	72229	137033	82994
Fraction of triggers used	38%	33%	31%	31%
LA tracks with ≥ 12 hits	68340	188754	464308	346856
Average multiplicity	2.3	3.5	4.7	6.0
Accepted momentum (vertex constraint)	50985	138261	338598	242114
From target and in kinematic region	34430	93220	214339	148012
Negative particles	3836	14485	42159	33095
Positive particles	30594	78735	172180	114917
π^- **selected with PID**	3526	13163	37706	29105
π^+ **selected with PID**	4706	15791	42296	31407

low dE/dx were used for this figure. Cuts are applied at $|d'_0| < 15$ mm and -14.4 mm $< s\, z'_0 < 20.0$ mm. The $\sin\theta$ dependence in the cut has been introduced to take into account the angular dependence of the precision of the extrapolation. The accepted $s\, z'_0$ region is symmetric around the centre of the target. The target extends from $z = 0$ to $z = 5.6$ mm in this coordinate system. The transverse coordinates of the interaction vertex are obtained extrapolating the trajectory of the incoming beam particle measured by the MWPCs. The longitudinal coordinate is taken from the position where the fitted track is closest to the trajectory of the beam particle.

Finally, only tracks with momentum in the range between 100 MeV/c and 800 MeV/c are accepted. In addition, particles with transverse momentum below 55 MeV/c are removed. This range meets the requirements of the data needed for the design of the neutrino factory and is consistent with the acceptance and resolution of the chamber. Table 1 shows the number of events and tracks at various stages of the selection. To give an impression of the complexity of the events, one can define an 'average multiplicity' as the ratio of the number of tracks with at least twelve hits in the TPC (regardless of their momentum, angle or spatial position) and the number of events accepted by the selection criteria with at least one such track. The average multiplicity obtained according to this definition is reported in Table 1.

5 Performance of the detector

The present measurement concentrates on the production of particles at large angles from the beam direction as measured in the TPC. To calibrate the performance of the TPC one would ideally enter particles of known momentum and type into the sensitive volume of the chamber. To achieve this either the chamber would have to be rotated or moved to another position or the beam would have to be steered far from its normal trajectory. Neither option was available so that other methods had to be employed to characterize the performance of the chamber. Cosmic-ray tracks and the elastic events in the data taken with hydrogen targets were used to characterize the TPC. Additional constraints were obtained making use of the characteristic momentum dependence of the dE/dx for particle tracks in the TPC.

The measured quantities used in the analysis are the momentum, scattering angle with respect to the beam particle and particle identification. Therefore, the performance of the detector needs to be characterized for these quantities and for the efficiency to reconstruct the tracks as a function of these quantities. In addition, the ability of the simulation to reproduce these has to be studied. The resolutions, measurement biases and efficiencies need to be known as function of the important kinematic variables.
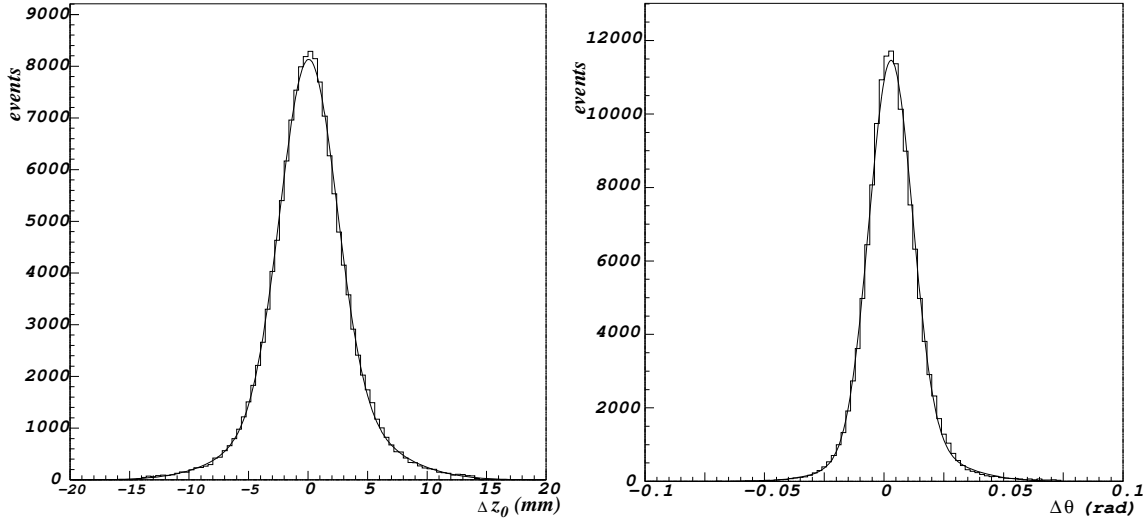
Figure 8: Left: Measurement with cosmic-ray tracks of the z'_0 resolution of the TPC. The distribution has an RMS of 3.4 mm. Right: measurement with cosmic-ray tracks of the θ resolution of the TPC. The distribution has an RMS of 12 mrad.

To investigate which fraction of the data can be used in the presence of dynamic distortions the behaviour of the quantities relevant for the analysis has been studied as a function of the strength of these distortions. As discussed above, the average d'_0 of the tracks produced by the beam in the target is used as a parameter to characterize the strength of the dynamic distortions.

It will be demonstrated that each important reconstructed quantity and its behaviour as a function of time in spill can be characterized using constraints from the data themselves. The absolute scale of the momentum is determined making use of the kinematics of elastic scattering. Its resolution is measured with cosmic-ray tracks with consistency checks based on dE/dx and elastic scattering. The evolution with the effect of dynamic distortions is measured with elastic scattering and dE/dx constraints, while the analysis of dE/dx sets a limit on any possible charge-asymmetry in the momentum measurement. Similarly, the resolution of the measurement of the scattering angle is obtained with cosmic-ray data, supported by consistency checks from elastic scattering. The absolute measurement of the angle and its sensitivity to dynamic distortions is constrained by the kinematics of elastic scattering. In the analysis, PID is based on the measurement of dE/dx. The robustness of the dE/dx measurement was observed with elastic scattering and with minimum-ionizing particles using the fact that the dE/dx is independent of the momentum measurement for these particles. The efficiency and purity of the identification of the particle type was measured using an independent selection based on time-of-flight. Finally, an absolute measurement of the efficiency and its evolution as a function of strength of the dynamic distortions was obtained with elastic scattering. The most important points will be elaborated below.

5.1 Study with cosmic-ray events

Cosmic-ray data were taken during and outside the beam data taking periods. During beam periods, cosmic-ray triggers were collected between the beam spills. Additional cosmic-ray exposures were performed close to the data taking periods with the beam to ensure that the detector conditions remained the same. For these data the outer barrel RPCs were used to provide a trigger for the cosmic-rays. In the year following data taking (2003) an extensive cosmic-ray exposure was performed providing a dedicated calibration. In particular, the trigger was provided by a scintillator rod positioned in the inner field cage to obtain tracks following the same trajectory as secondary tracks during beam exposures. The rod was placed at the nominal target position with transverse dimensions similar to the beam spot size, but more extended in z than the usual targets.

The resolution of the extrapolated track position at the target was measured by splitting the cosmic-ray track into two halves and taking the distance between the two extrapolated trajectories. The difference in the extrapolation in the direction of the beam measures the z'_0 resolution. Figure 8 (left) shows the result of this measurement. The distribution has an RMS of 3.4 mm. The resolution in the angle of secondary tracks with respect to the beam direction θ can be measured again by comparing the two track segments. The resolution measured in this way is shown in the right panel of Fig. 8. The distribution has an RMS of 12 mrad. The mean value is non-zero, reflecting a small systematic uncertainty in the measurement of θ of the order of 5 mrad. This bias is caused by the limited precision of the equalization constants of the pad pulse heights which can introduce an r-dependent systematics in the determination of the z-position of hits. In the absence of interactions by beam particles the equalization constants determined for the cosmic-ray data-taking periods are expected to be less precise than for the normal data-taking periods. This effect has been found to induce a negligible uncertainty in the analysis.

To measure the transverse momentum resolution three estimates of the transverse momentum of the cosmic-ray track are obtained: the transverse momentum measured from the curvature of the two halves of the track separately and the transverse momentum from the curvature of the complete track. The relative resolution is then obtained from the distribution of the difference of the inverse of the transverse momenta of the two half-tracks divided by the inverse of the overall track transverse momentum. The sigma of the Gaussian fit (divided by the square-root of two) is plotted as a function of the transverse momentum of the overall track. The result of this analysis is shown in Fig. 9. Since the resolution is expected to be Gaussian in the curvature $(1/p)$, the resolution is shown in this quantity. The resolution measured with cosmic-rays is compared with the over-estimates which can be obtained by selecting a small slice of the steep part of the dependence of the dE/dx on the momentum[3]. Subdividing the data-sample into different bins of θ a fixed dE/dx slice (corresponding to a given momentum) can be used to determine several points at different p_T. The resolution expected from the simulation using the point–to–point resolution measured with dE/dx in the data is consistent with the cosmic-ray measurement. We do observe, however, a slightly larger constant term in the cosmic-ray data as predicted by the simulation. In the 2003 data the cosmic-ray tracks were triggered by a scintillator on the TPC axis. The amount of material of the scintillator is similar to the amount of material in the inner field cage and trigger detector. Hence, the constant term is expected to be slightly larger for the cosmic-rays than for the MC. In the 2002 data, no such trigger detector was available. Therefore the tracks do, in majority, not pass the nominal axis of the TPC, such that they see effectively a larger amount of the inner field cage material.

5.2   Study with elastic scattering data

Elastic scattering interactions of protons and pions on hydrogen provide events where the kinematics are fully determined by the direction of the forward scattered beam particle. The kinematic properties of the elastic scattering reaction were exploited to provide a known 'beam' of protons pointing into the TPC sensitive volume. Data were taken with liquid hydrogen targets at beam momenta from 3 GeV/c to 15 GeV/c. A good fraction of forward scattered protons or pions in the elastic scattering reaction enter into the acceptance of the forward spectrometer. The full kinematics of the event can be constrained by a precise measurement of the direction of the forward scattered beam particle. In particular, the direction and momentum of the recoil proton are precisely predicted. Selecting events with one and only one track in the forward direction and requiring that the measured momentum and angle are consistent with an elastic reaction already provides an enriched sample of elastic events. By requiring that only one barrel RPC hit is recorded at the position predicted for an elastic event (the precision of the prediction from the forward spectrometer is within the RPC pad size) and within a time window consistent with a proton time-of-flight a sample of recoil protons with known momentum vector of a purity of about 99% is obtained. At beam momenta in the range 3 GeV/c–8 GeV/c the kinematics are such that these protons point into the TPC with angles of $\approx 70°$ with respect to the beam direction. Once a clean sample of elastic-scattering events is isolated the efficiency of the track finding and fitting procedure can be measured and an estimate of the resolution and biases of the measurement of momentum and angle can be obtained. The correlation of the forward scattering angle and recoil proton momentum is such that

---

[3]The momentum resolution is over-estimated since the effects of the size of the dE/dx slice and the dE/dx resolution are not corrected for.
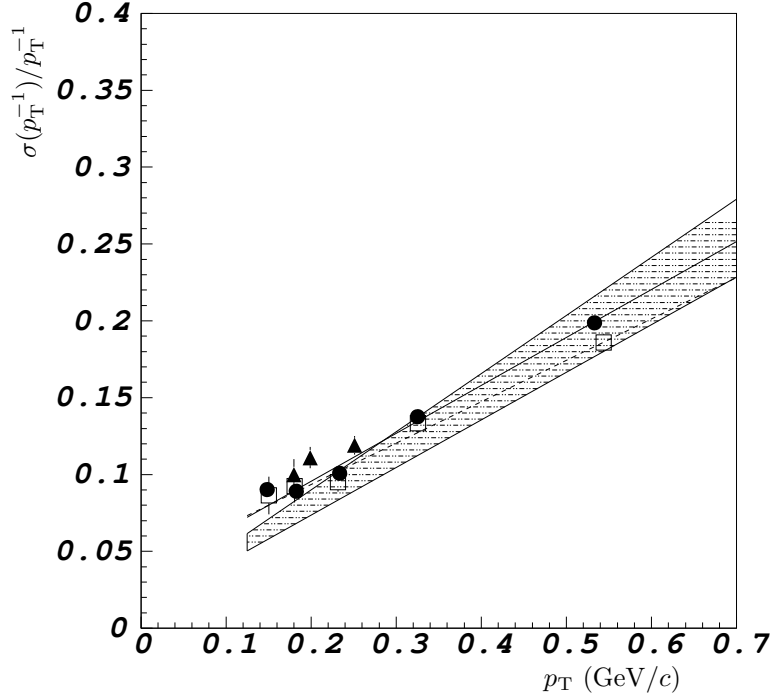
Figure 9: Momentum resolution in the TPC. The filled circles (open boxes) and the drawn (dashed) straight line refer to the cosmic-ray data taken in 2003 (2002). The filled triangles are the upper limits ('over-estimates') obtained from the dE/dx selection. The shaded area refers to a straight-line fit to the Monte Carlo calculations.

an unavoidable threshold in recoil proton momentum (≈ 350 MeV/c) translates into a minimum angle for the scattered particle. The threshold is relatively high due to the need to detect the proton also in the barrel RPC system outside the outer field cage of the TPC. This requirement can be removed only in cases where a small amount of background can be tolerated. Due to the geometry of the rectangular aperture of the dipole magnet of the forward spectrometer only two small horizontal sectors of the TPC can be populated with recoil protons above threshold momentum in the 3 GeV/c beam. In the 5 GeV/c beam the situation is much better and all azimuthal angles can be populated, although not yet homogeneously. In the 8 GeV/c beam the population is homogeneous in ϕ, but the error propagation of the measurement of the forward scattering angle into the prediction of momentum and angle of the recoil proton becomes less favourable. Summing up all these arguments, the 8 GeV/c beam is most suitable for the determination of average efficiency, the 5 GeV/c beam is still useful for efficiency measurements and provides a good sampling of the resolution of the detector, while the 3 GeV/c beam can be used to study the resolution with the most favourable situation for the prediction. The numbers of selected elastic events total about 15,000 for the 8 GeV/c data sample, and 5,000 for the 5 GeV/c and 3 GeV/c data samples each.

Based on the 8 GeV/c data the track reconstruction efficiency was determined to be $91\% \pm 1\%$ compared with an efficiency of 93% calculated with the simulation. In the 5 GeV/c beam the efficiency is the same as that for 8 GeV/c data. In the data a $\approx 1\%$ loss of efficiency can be attributed to channels with intermittent connection problems, an effect not simulated in the Monte Carlo (MC). The inefficiency is dominated by the effect of the 'spokes', the place where the wires of the wire-planes are fixed as shown in Fig. 10 (left). The integral of the efficiency is well reproduced, although the details near the spoke are different. This is due to the smearing effect in the measurement of ϕ under the influence of dynamic distortions. Since the analysis is performed integrating over ϕ this has to first order no effect. The good agreement of the measurements of the absolute efficiency with the simulation justifies the use of the simulation to determine the efficiency to measure pions. The systematic error is estimated by changing the effective cut on the number of points to accept tracks.

Figure 10 (right) displays the results of this analysis for the reconstruction with and without vertex
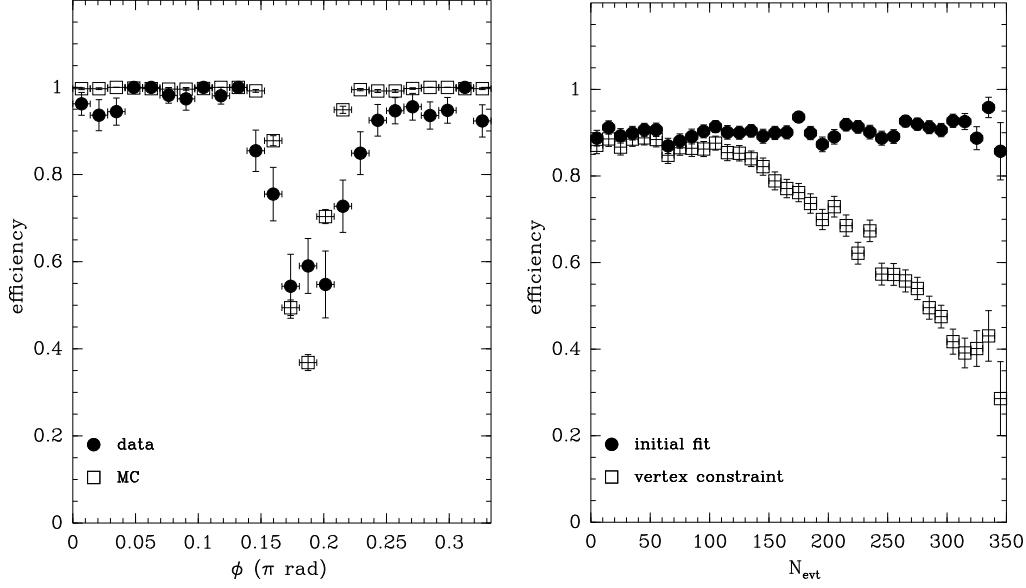
Figure 10: Left panel: the track finding efficiency as a function of ϕ within the sectors of the pad-plane of the TPC for 8 GeV/c elastic scattering data measured with elastic events (first 80 events in the spill). The filled circles show the efficiency for recognizing tracks including the fit to a helix in the data, the open squares show the simulated efficiency. The integral of the efficiency is well reproduced, although the details near the spokes are different. Right panel: Efficiency for the pattern recognition and momentum reconstruction for elastically produced recoil protons as a function of event number in spill. Closed circles: trajectory fit without vertex constraint; open squares: trajectory fit with vertex constraint. The efficiency includes the effect of the cut on d_0'. The efficiency for the reconstruction and fit using the vertex constraint remains constant within $\approx 1\%$ up to a distortion corresponding to $\langle d_0' \rangle = 6$ mm.

constraint. The efficiency of the reconstruction without vertex constraint is insensitive to distortions (*i.e.* the track will be found and measured), while the momentum reconstruction using the vertex constraint keeps a constant efficiency up to $N_{\mathrm{evt}} \approx 90$, corresponding to $\langle d_0' \rangle \approx 6$ mm for this data set. The loss of efficiency for the constrained fit is due to the need to apply a cut in d_0' to ensure that the track originates from the vertex. It can therefore be concluded that the efficiency for the reconstruction and fit using the vertex constraint remains constant within $\approx 1\%$ up to a distortion corresponding to $\langle d_0' \rangle = 6$ mm.

It was verified with the data that the value of θ is not modified by the dynamic distortions. However, the momentum estimated with the fit not using the impact point of the incoming beam particle and the value of d_0' is biased as a function of event in spill due to the effect of these distortions as shown in Fig. 11. The results of this analysis justify the use of only a limited number of events in each spill in order not to introduce large uncertainties due to distortions. The analysis of the elastic scattering events sets very stringent constraints on the maximum effect of distortions of all kinds on the measurements of kinematic quantities with the TPC. Therefore, solid estimates for the magnitude of the systematic error sources are obtained. For the hydrogen runs a higher beam intensity was used roughly equalizing the interaction rate between these runs and the runs with a tantalum target. In fact, the dynamic distortion effects were in strength similar to the 12 GeV/c Ta runs. Since the analysis takes into account this variation by applying a cut at a different value of N_{evt} the measurements are representative for all datasets[4].

The resolution in the measurement of the polar angle θ is shown in Fig. 12 as a function of the predicted momentum of the proton when it enters the gas. The comparison of the experimental result with the simulation shows good agreement. For low-momentum protons ($p < 500$ MeV/c) the resolution is dominated by multiple scattering.

Since the energy loss in the material of the cryogenic target, trigger counter, and inner field cage is large

---

[4]The value of "maximum N_{evt}" reported in Table 1, can be used to estimate a value of equal strength of dynamic distortions for different datasets.
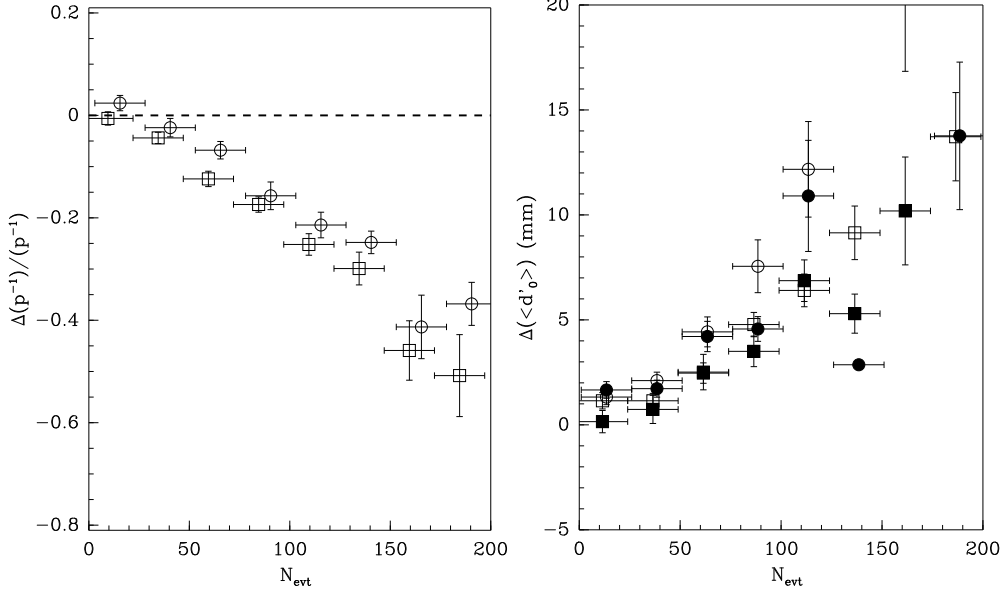
Figure 11: Left panel: The shift in average momentum for elastic scattering data (3 GeV/c: open squares, 5 GeV/c: open circles) measured with elastic events as a function of the value of N_{evt}. The momentum estimator from the fit not constrained by the impact point of the incoming beam particle is used here. Right panel: The shift in average d'_0 as a function of the event number in spill for elastic scattering data (3 GeV/c: filled and open boxes, 5 GeV/c: filled and open circles) measured with elastic events as a function of the value of N_{evt}. The open symbols show the data for predicted momenta below 450 MeV/c and the filled symbols for predicted momenta above 450 MeV/c.
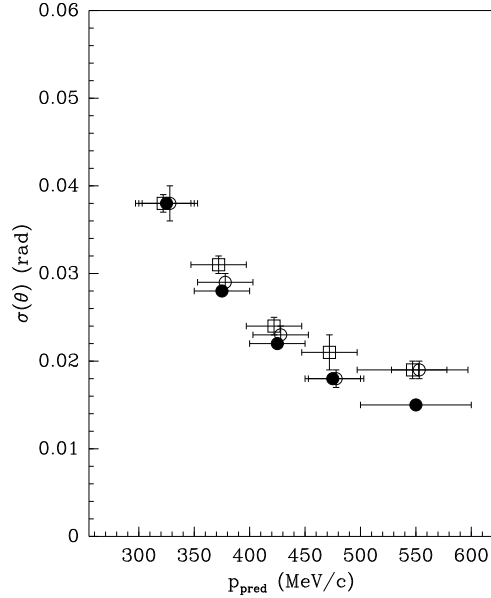

Figure 12: The resolution in θ for elastic scattering (3 GeV/c: open boxes, 5 GeV/c: open circles) data measured with elastic events as a function of the momentum predicted by the forward scattered track compared to a simulation of the same sample of events at 5 GeV/c (filled circles).
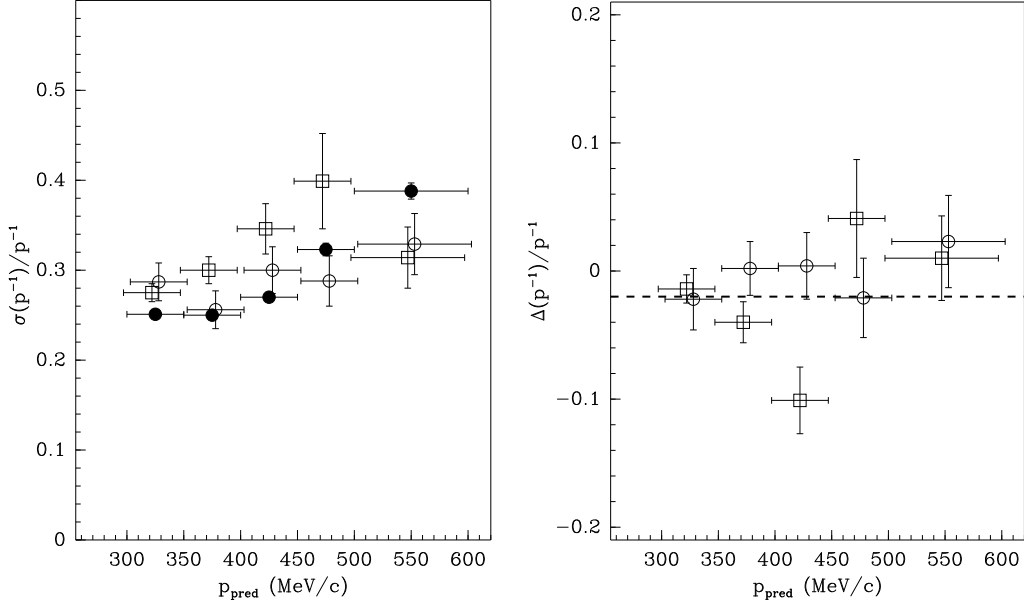
Figure 13: Left panel: The momentum resolution of the fit without vertex constraint for elastic scattering data (3 GeV/c: open squares, 5 GeV/c: open circles) measured with elastic events as a function of the momentum predicted by the forward scattered track. The resolution is dominated by the effect of energy-loss and multiple scattering and is consistent with the measurement with cosmic-ray tracks. The filled circles show a full simulation of the elastic events using a realistic elastic cross-section model and detector description. The agreement between data and simulation is good. Right panel: the momentum bias of the fit without vertex constraint measured with elastic scattering data (3 GeV/c: open squares, 5 GeV/c: open circles) with elastic events as a function of the momentum predicted by the forward scattered track. In the absence of a clear trend, the average of the points constrains the bias to be smaller than 3%. For these comparisons only the first 50 events in the spill are used since the unconstrained fit is sensitive to dynamic distortions beyond this value.

for protons in the energy range covered by elastic scattering, there is a significant change of curvature of the trajectory of these protons in that region of the detector. This effect could introduce a bias in the measurement of the momentum using the vertex constraint for these low-momentum protons. Therefore, it is more significant to study the behaviour of the momentum measurement for protons without making use of the vertex constraint. For pions, it was checked independently that the constrained fit is unbiased with respect to the unconstrained fit for tracks reconstructed in the data and the simulated data. The momentum measured for recoil protons in elastic scattering events using the fit without vertex constraint is compared with the prediction based on the forward scattering angle including a correction for energy-loss in the liquid hydrogen target and the material surrounding the target (including the trigger counter and inner field cage). The comparison is made in the variable $1/p$. The measurement of the momentum resolution of the fit without vertex constraint is shown as a function of momentum in Fig. 13 (left). Although the resolution is consistent with the measurement with cosmic-ray tracks, this is not a very strong constraint since it is dominated by the effect of energy-loss and multiple scattering. The simulation predicts for protons a resolution of $\approx 30\%$ in the range from 300 MeV/c to 600 MeV/c. The momentum bias using the fit without vertex constraint is shown as function of predicted momentum in Fig. 13 (right). The average of the bias is $(2 \pm 1)\%$. In the absence of a clear trend one concludes that the bias is less than 3%. From the precision in knowledge of the absolute beam momentum and the precision in the measurement of the kinematical quantities of the forward scattered track one cannot expect a precision better than 2% in this cross-check. For this comparison only the first 50 events in the spill are used in order to avoid the effect of dynamic distortions in the unconstrained fit as shown in Fig. 11.

Since the behaviour of the fit constrained with the impact point of the incoming beam particle cannot be studied very well using low momentum protons, the effect of distortions on this estimator is studied using other physical benchmarks. These will be described in the following section. The fact that the
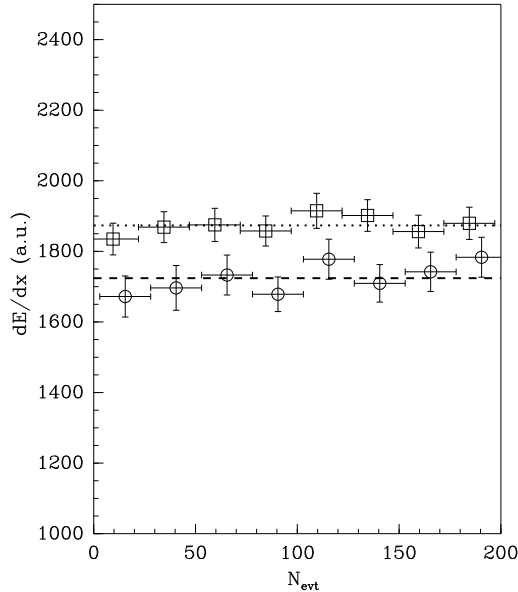
Figure 14: The average value of dE/dx as a function of the event number in spill for elastic scattering data (3 GeV/c: open boxes, 5 GeV/c: open circles) measured with elastic events. The dotted and dashed lines show the average value for 3 GeV/c and 5 GeV/c, respectively.

measurement of dE/dx is insensitive to the distortions will be used in these studies. The robustness of this quantity can be observed in Fig. 14. The average dE/dx is shown as a function of event number in spill for the sample of elastic events selected using the forward spectrometer. The definition of the sample is independent of measurements in the TPC. Both in the 3 GeV/c and 5 GeV/c beam this quantity is stable. The higher average dE/dx in the 3 GeV/c beam is caused by the lower average momentum of the protons.

5.3 Systematic checks of the momentum measurement

In Fig. 15 the sensitivity of the momentum measurement to dynamic distortions is shown. Particles were selected in narrow bands of dE/dx in regions where dE/dx depends strongly on momentum. To select a sample with the highest possible momentum, the protons in the right panel of Fig. 15 were required to reach the RPC system (low momentum protons would be absorbed before reaching the RPCs) in addition to the requirement $dE/dx > 4.8$ MIP. A further selection 1.0 rad $< \theta < 1.5$ rad ensures a limited range of p_T. The same angular selection was applied for the tracks shown in the left panel, together with a selection 2.3 MIP $< dE/dx < 2.8$ MIP. Owing to the combined selection of a dE/dx interval and momentum interval, the sample of tracks in the left panel of Fig. 15 is a pure pion sample and in the right panel of the same figure a pure proton sample. The analysis was performed for the combined data set taken with 3 GeV/c, 5 GeV/c, 8 GeV/c and 12 GeV/c beams on Be, C, Cu, Sn, Ta and Pb targets. As can be seen in Fig. 15 the momentum measurement using the vertex constraint is robust with respect to the dynamic distortions within a few percent for values of $\langle d_0' \rangle$ smaller than 5 mm. This robustness is contrary to the effect observed with the fit not using the vertex constraint which is much more sensitive to distortions as shown in Section 5.2. The average momentum obtained from a Gaussian fit to the momentum distribution shows that the average momentum stays constant within a few percent up to $N_{evt} = 200$ at $p_T \approx 95$ MeV/c (pions) and up to $N_{evt} = 100$ at $p_T \approx 350$ MeV/c (protons), respectively. For this data set $\langle d_0' \rangle$ is ≈ 5 mm at $N_{evt} = 100$ and roughly twice as large at $N_{evt} = 200$. The p_T-range covered by this cross-check represents a large range of the kinematic domain used in the analysis. It is expected that the transverse momentum measurement of lower p_T tracks ($p_T \approx 95$ MeV/c) is less affected by dynamic distortions than that of higher p_T tracks ($p_T \approx 350$ MeV/c) since an equal shift in position of the clusters induces a smaller fractional change in curvature for tracks with large curvature.
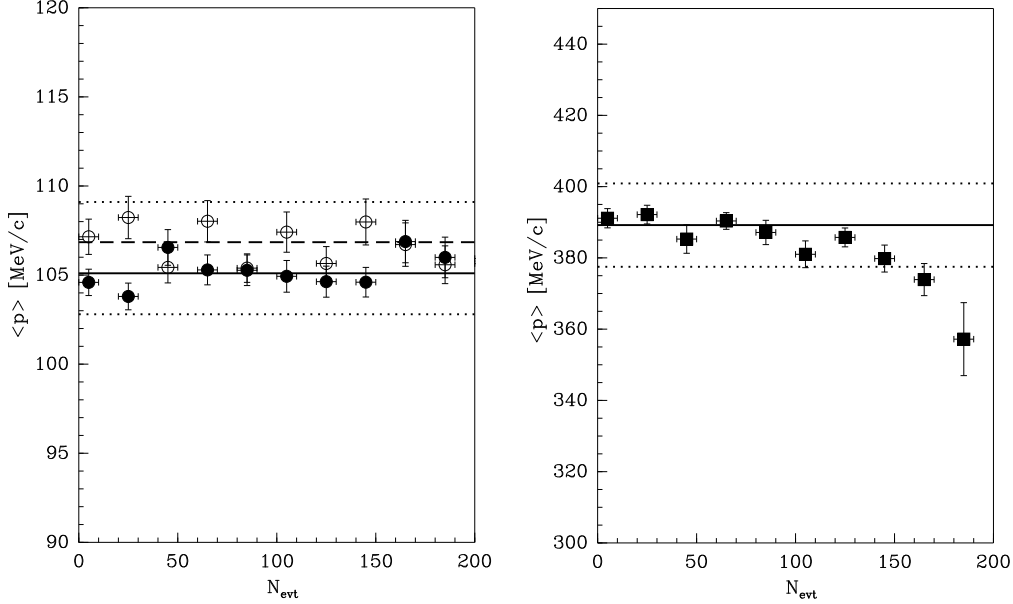
Figure 15: Comparison of the average reconstructed momentum as a function of event number in spill: left, for charged pions selected using dE/dx, open circles are for π^-, closed circles are for π^+; right, for protons using a higher value of dE/dx for the selection. In the left panel the straight lines indicate the average values for the first 100 events: dashed line for π^- and solid line for π^+. In the right plot the solid line shows the average for protons for the first 100 events. The dotted lines in both panels show the $\pm 3\%$ variation around the averages. For both panels a selection 1.0 rad $< \theta < 1.5$ rad was applied to ensure a limited range of $p_{\rm T}$. For the protons in the right panel the requirement that they have a hit in both barrel RPC layers was applied to set a momentum threshold.

The measurement of the angle of the particles' trajectory with respect to the beam direction θ remains constant within a few mrad up to $\langle d_0' \rangle = 10$ mm.

To check asymmetries of the momentum reconstruction between π^+ and π^- one can inspect the results of the analysis where tracks emitted almost perpendicular (1.0 rad $< \theta < 1.5$ rad) to the beam direction with a dE/dx of about three times the value of a minimum ionizing particle were selected. Using the fact that the π^+ and π^- spectra are expected to be similar at these angles and that the dE/dx selection keeps only pions in a narrow momentum region, one can constrain reconstruction asymmetries. For this selection we find an average pion momentum of 105 MeV/c with an asymmetry of 1%, as shown in Fig. 15. This is negligible compared to other systematic errors in the analysis (see Section 5.2).

5.4 Efficiency

Having verified the ability of the Monte Carlo program to simulate the efficiency for protons (Section 5.2), the simulation is then used for pions. The efficiency calculation was done by simulating single π^+ and π^- in bins of θ and p. The map of dead channels in the TPC was applied corresponding to the data set to be corrected. Thus a different simulation was run for each of the momentum settings. The same cuts used for the data were applied to the reconstructed MC tracks. Figures 16 (left) and 16 (right) show the efficiency for pions as a function of p and θ, respectively. The variable on the abscissa in Fig. 16 (left) is the momentum of the pion in the gas of the TPC, hence after energy loss in the target and the material around the inner field cage. The result confirms that the efficiency is strongly limited at low momentum ($p \leq 75$ MeV/c for pions) due to the energy-loss in the materials surrounding the target and inside the target itself. Consequently, the measurement will be limited to pions with momentum at their production point above 100 MeV/c. The dip at $\theta = 1.57$ rad ($0.5\ \pi$ rad) in Fig. 16 (right) is due to the absorption and energy loss in the target. The amount of material represented by the target with its 30 mm diameter is large for tracks traversing it at 90 degrees with respect to the beam direction. This effect dominates
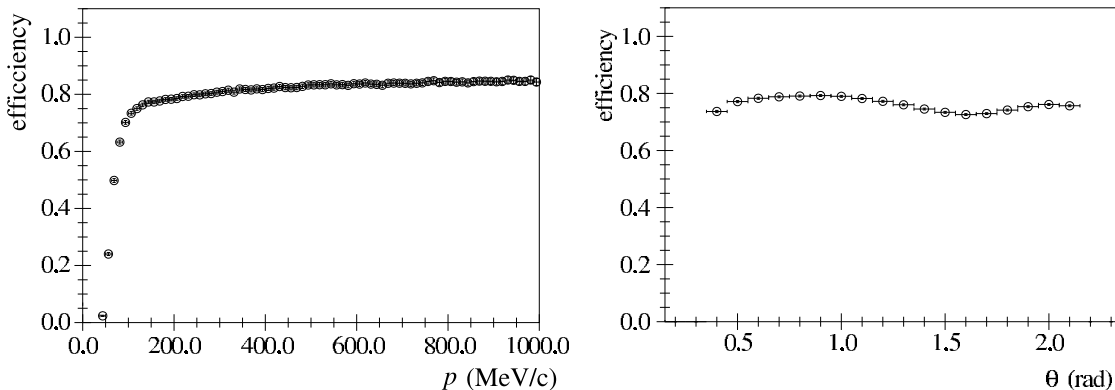
Figure 16: Left: the efficiency as a function of total momentum at their production point for pions. Right: the efficiency as a function of θ for pions.

over the increase in material seen by tracks which traverse the inner field cage at small angles with respect to the beam, but which traverse only on average half of the 5.6 mm thickness of the target in the beam direction.

5.5 Particle identification

The particle identification in the large-angle region mainly uses the dE/dx information provided by the TPC. The measurement of dE/dx is shown as a function of momentum in Fig. 17. The electron, pion and proton populations are well separated at most momentum values. As an example, the distributions in various momentum ranges are shown in Fig. 18 and 19. These figures show the separation between electrons and pions in the low momentum region, and the pion–proton separation at intermediate and higher momenta. Fits with two Landau distributions (corresponding to the different particle types) are also shown in the figures. In this analysis simple momentum dependent cuts are used to separate the different populations. The pions are identified by removing electrons and protons. The kaon population is negligible. The cuts were optimized to maximize the purity of the pion sample, accepting a lower efficiency in the selection.

The measurement of the velocity β of secondary particles by the time-of-flight determination with the RPC detectors using the BTOF as starting-time reference provides complementary particle identification. It allows the efficiency and purity of the PID algorithm using dE/dx to be studied for a large subset of the TPC tracks. Combining the samples taken with the different beam momenta used in this analysis a statistical accuracy of the order of 0.2% can be obtained in the PID efficiency determination.

The choice to use dE/dx as principal PID estimator is motivated by two facts. The first argument is given by the fact that dE/dx is obtained as a property of the same points which constitute the TPC track, while the TOF is obtained by matching the track to an external device. It is observed that the background in the matching is not negligible. Converted photons from π^0 production can hit the same – rather large – RPC pad as the one pointed to by the track. This background depends on the position in the RPC barrel where the pad is located and is different for every momentum setting. Thus a different background subtraction would have to be determined for each momentum–target dataset. The second argument is the increased complexity of the analysis which would be introduced by having to combine two PID detectors of which the response is highly non-Gaussian. The probability density functions of both the response of the dE/dx and of the TOF would have to be determined as function of all relevant parameters. The gain in efficiency one would obtain with such a procedure would be rather limited and would not balance the additional systematics introduced. On the contrary, the availability of an independent PID device makes it possible to determine the efficiency and purity of the selection with the main device in a straightforward manner, without the need to know the efficiency of the independent auxiliary PID device.
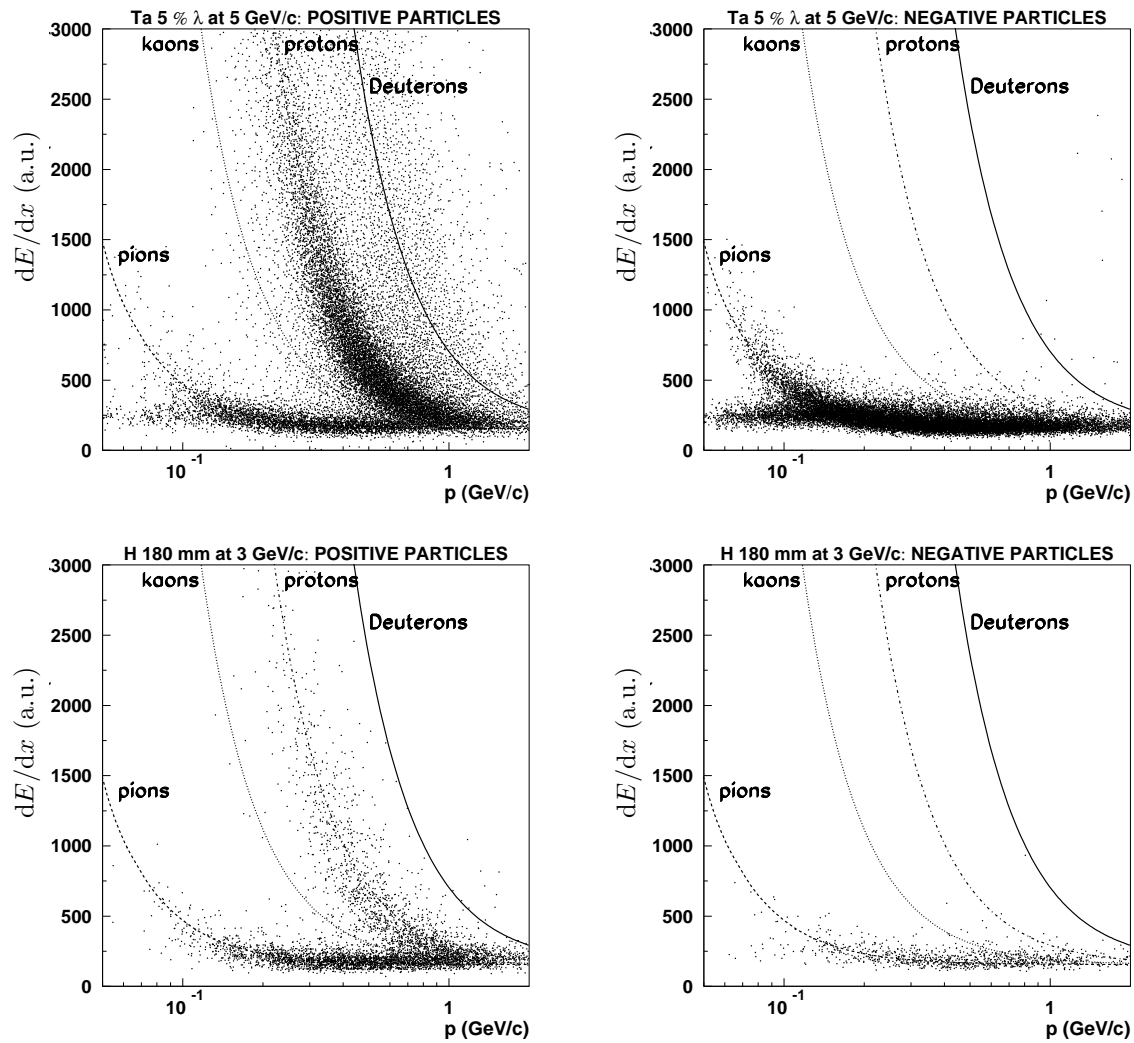
Figure 17: $\mathrm{d}E/\mathrm{d}x$ (in arbitrary units) versus momentum (in GeV/c). Top: p–tantalum data in the 5 GeV/c beam; Bottom: p–hydrogen data in the 3 GeV/c beam; Left: for positive tracks; Right: for negative tracks. The lines are simple β^{-2} curves and merely indicate the regions populated by the various particle types. The fact that the band marked 'deuterons' is not present in the hydrogen data clearly shows that the population in this band in the tantalum data is not an artefact of the momentum reconstruction but deuteron production.
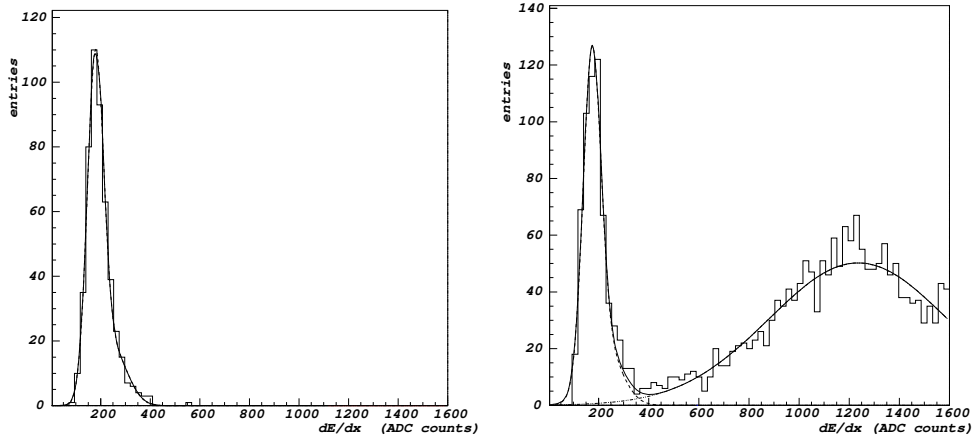
Figure 18: dE/dx spectra for negative particles (on the left) and positive (on the right) with momentum between 300 MeV/c and 350 MeV/c. The curves show the Landau distributions fitted to the data. The protons are clearly visible in the distribution for positive particles at high dE/dx and absent for the negatively charged particles.
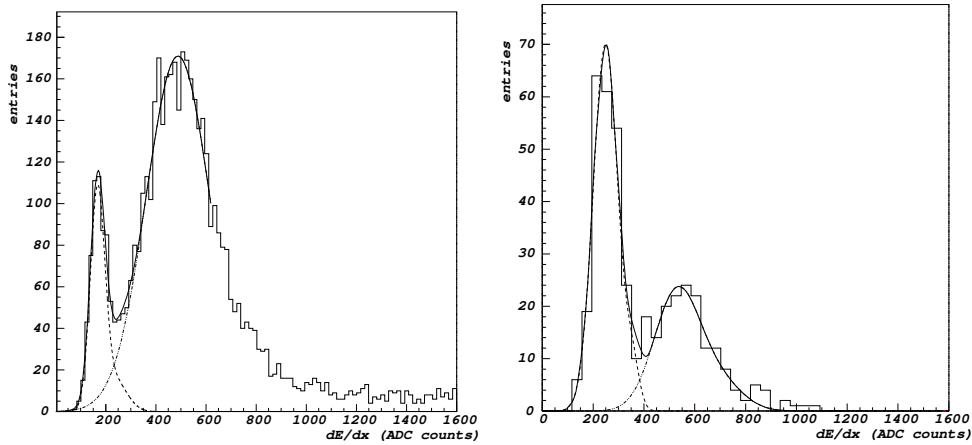
Figure 19: Left panel: dE/dx spectra for positive particles with momentum between 500 MeV/c and 600 MeV/c. The curves show the Landau distributions fitted to the data. The distributions of pions and protons are distinct but not cleanly separated. Right panel: The dE/dx spectrum for negative particles with momentum between 75 MeV/c and 100 MeV/c. The curves indicate the fits to the two components using two Landau distributions. The distribution of the electrons with low dE/dx is clearly visible to the left of the highly ionizing negative pions.
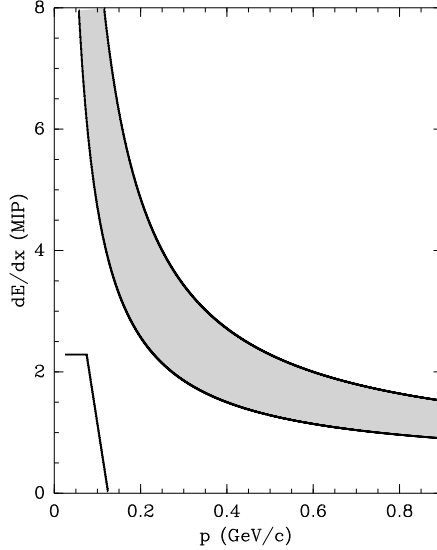
Figure 20: Criteria used for the PID selection using the dE/dx (expressed in MIP) as a function of the measured momentum of the particle. Low momentum electrons and positrons are rejected when their dE/dx is below the lower left curve. The remaining paricles are classified as protons if their dE/dx is above the gray band, as pions if they are below the gray band and rejected when they lie inside the gray band. The value of the MIP is calibrated for each setting.

The measurement of β allows an almost independent selection of a very pure proton sample to be made in the momentum range 300 MeV/c–800 MeV/c with a purity better than 99.8%. The purity of the sample was checked using negative particles and verifying that no particles identified as anti-protons are present. While a proton sample was obtained using interactions of incoming protons, a pure pion sample was prepared by using negative pions selected by TOF produced by incident positive pions. The behaviour of positive pions was also checked for momenta below 500 MeV/c (where they can be selected without proton contamination) and was found to be equal to that of negative pions.

The cuts were defined favouring purity over efficiency and are shown graphically in Fig. 20. Protons are selected by requiring a high dE/dx, while at higher momenta pions are selected with low dE/dx. To ensure purity of both samples there are 'unidentified' particles between the two samples. At low momenta electrons are rejected by selecting low dE/dx, while pions are accepted with a higher dE/dx. This separation is not pure above 125 MeV/c, so an electron subtraction is needed in the analysis.

The result of this analysis in terms of efficiency and of the fraction misidentified particles is shown in Fig. 21. For the pions, the drop in efficiency toward higher momenta is caused by the need to make a hard cut to remove protons. The migration of pions and protons into the wrong sample is kept below the percent level in the momentum range of this analysis ($p < 800$ MeV/c). This is important for the measurement of the π^+ production rate since the proton production rate is five to ten times larger in some of the bins. The small differences in efficiency (up to $\approx 5\%$) which are visible between the data and the simulation are dealt with in the analysis by an *ad hoc* correction to the cross-sections. It is checked that the angular dependence of the PID efficiency and purity are negligible.

With the cuts as described above, the momentum distributions of pions are obtained in angular bins (indicated in mrad in the panels) as shown in Fig. 22. The distributions in this figure are not corrected for efficiencies and backgrounds.

5.6 Simulation program

The experiment simulation is based on the GEANT4 toolkit [29]. The materials in the beam line and the detector are accurately reproduced in this simulation, as well as the relevant features of the detector
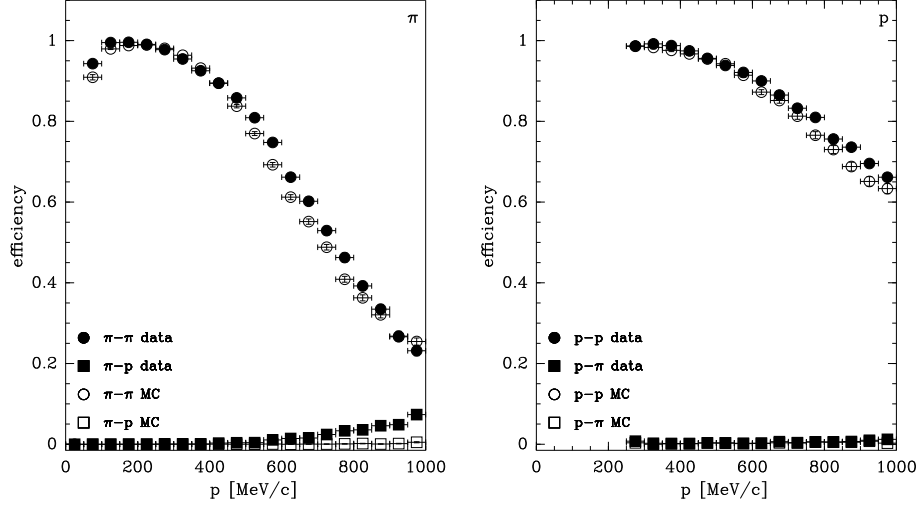
Figure 21: Performance of the PID using the dE/dx as a function of the measured momentum of the particle. The particles are selected using TOF. Left: for negative pions produced in a positive pion beam; Right: for protons produced in a proton beam. The filled (open) circles show the efficiency measured with the data (Monte Carlo), the filled (open) squares represent the fraction of particles misidentified as anti-protons (left) and pions (right) in the data (Monte Carlo).

response and the digitization process. The simulation starts from a beam proton 4.5 m upstream of the tantalum target. The characteristics of the proton beam are reproduced from the measurements with the MWPC for each momentum setting of the beam separately. The response of the relevant beam detectors is simulated in terms of measurements of time, position and direction, so that the reconstruction of simulated events gives realistic results.

The most important detectors to simulate for this analysis are the TPC, the RPC system and the trigger counters. In the TPC all stochastic processes in the energy deposition of the particles along their trajectories are reproduced, including the electron drift, the signal formation on the pad plane, the response of the electronics and the digitization process. Important details such as the individual behaviour of each single electronics channel in terms of pulse shape and signal amplitude are taken into account. For each different setting (beam–target combination) the precise knowledge of dead pads and equalization constants as observed in the data are reproduced. The RPCs are simulated using their actual geometrical details, and the response is reproduced from the overall performance observed in the data.

All relevant physical processes are simulated using the GEANT4 tools, including multiple scattering, energy-loss, absorption and re-interactions.

6 Analysis procedure

The double-differential cross-section for the production of a particle of type α can be expressed in the laboratory system as:

$$\frac{\mathrm{d}^2\sigma_\alpha}{\mathrm{d}p_i\mathrm{d}\theta_j} = \frac{1}{N_{\mathrm{pot}}}\frac{A}{N_A\rho t}M^{-1}_{ij\alpha i'j'\alpha'} \cdot N^{\alpha'}_{i'j'} \ , \tag{1}$$

where $\frac{\mathrm{d}^2\sigma_\alpha}{\mathrm{d}p_i\mathrm{d}\theta_j}$ is expressed in bins of true momentum (p_i), angle (θ_j) and particle type (α). The summation over reconstructed indices $i'j'\alpha'$ is implied in the equation. The terms on the right-hand side of the equation are as follows.
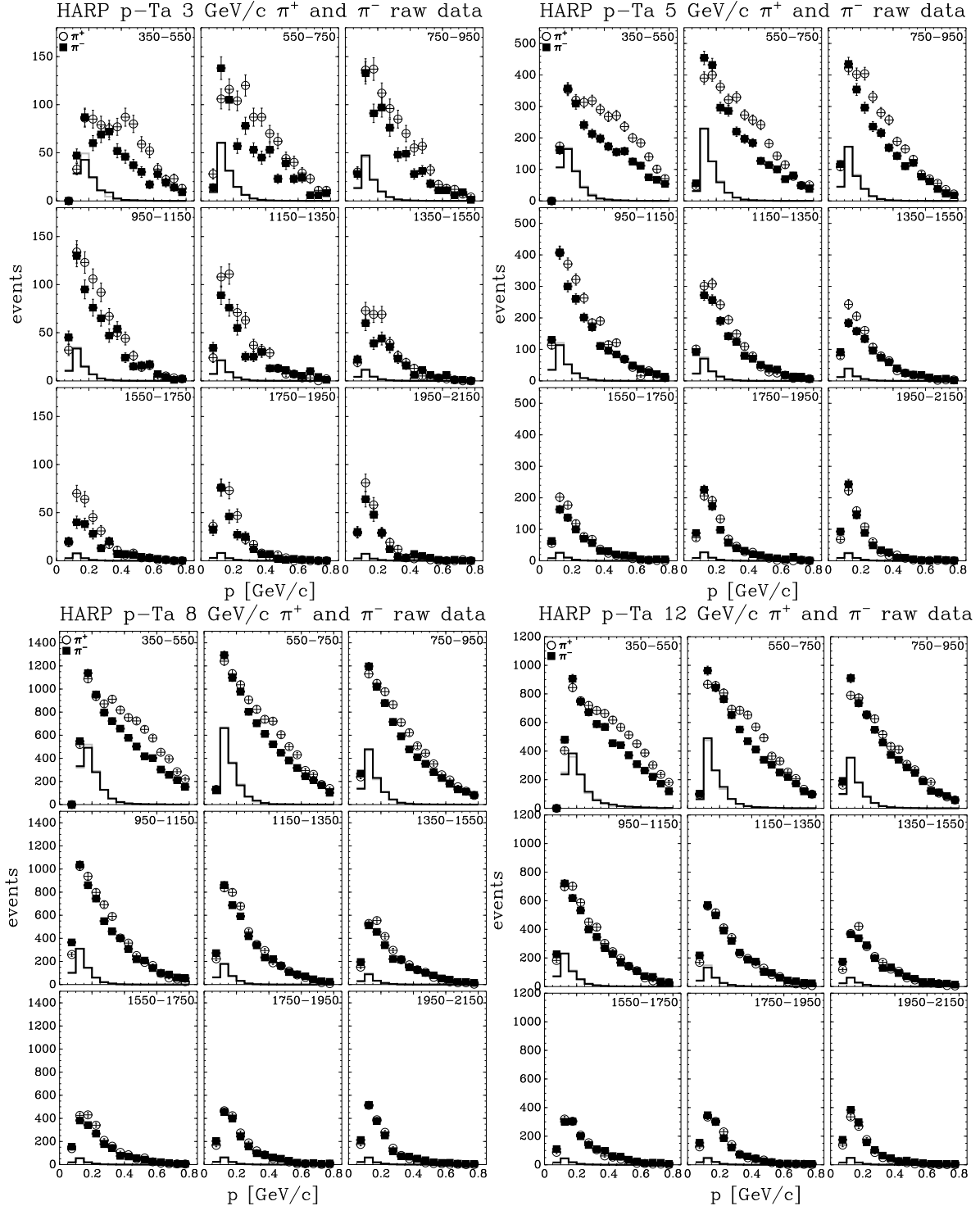
Figure 22: Distribution for positive (open circles) and negative pions (filled squares) using the PID algorithm based on dE/dx as a function of momentum and in different angular bins (indicated in mrad in the panels) taken with 3 GeV/c, 5 GeV/c, 8 GeV/c and 12 GeV/c proton beam hitting a tantalum target. The histograms show the distributions calculated for the π^0 subtraction (see Section 6). The shaded (black) lines show the positrons (electrons) to be subtracted from the π^+ (π^-) spectra. The two sets of lines coincide almost everywhere as expected from the production mechanism and are therefore almost indistinguishable in the figure.

The so called 'raw yield' $N_{i'j'}^{\alpha'}$ is the number of particles of observed type α' in bins of reconstructed momentum ($p_{i'}$) and angle ($\theta_{j'}$). These particles must satisfy the event, track and PID selection criteria.

The matrix $M_{ij\alpha i'j'\alpha'}^{-1}$ corrects for the efficiency and resolution of the detector. It unfolds the true variables $ij\alpha$ from the reconstructed variables $i'j'\alpha'$ and corrects the observed number of particles to take into account effects such as trigger efficiency, reconstruction efficiency, acceptance, absorption, pion decay, tertiary production, PID efficiency, PID misidentification and electron background. The method used to correct for the various effects will be described in more detail in the following section.

The factor $\frac{A}{N_A \rho t}$ is the inverse of the number of target nuclei per unit area (A is the atomic mass, N_A is the Avogadro number, ρ and t are the target density and thickness)[5].

The result is normalized to the number of incident protons on target N_{pot}.

Although, owing to the stringent PID selection, the background from misidentified protons in the pion sample is small, the pion and proton raw yields ($N_{i'j'}^{\alpha'}$, for $\alpha' = \pi^-, \pi^+, \text{p}$) have been measured simultaneously. This makes it possible to correct for the small remaining proton background in the pion data without prior assumptions concerning the proton production cross-section.

6.1 Correction for resolution, energy-loss, efficiency and backgrounds

Various techniques are described in the literature to obtain the matrix $M_{ij\alpha i'j'\alpha'}^{-1}$. In this analysis an unfolding technique is used. It performs a simultaneous unfolding of p, θ and PID, with a correction matrix M^{-1} computed using the Monte Carlo simulation.

A Bayesian technique, described in Ref. [30] is used to calculate the unfolding matrix. The central assumption of the method is that the probability density function in the ('true') physical parameters ('physical distribution') can be approximated by a histogram with bins of sufficiently small width. A population in the physical distribution of events in a given cell $ij\alpha$ generates a distribution in the measured variables, $M_{ij\alpha i'j'\alpha'}$, where the indices $ij\alpha$ indicate the binning in the physical angular, momentum and PID variables, respectively, and $i'j'\alpha'$ the binning in the measured variables. Thus the observed distribution in the measurements can be represented by a linear superposition of such populations. The task of the unfolding procedure consists then of finding the number of events in the physical bins for which the predicted superposition in the measurement space gives the best description of the data. The application of this unfolding method is described in Ref. [31].

In order to predict the population of the migration matrix element $M_{ij\alpha i'j'\alpha'}$, the resolution, efficiency and acceptance of the detector are obtained from the Monte Carlo. This is a reasonable approach, since the Monte Carlo simulation describes these quantities correctly (see Section 5). Where some deviations from the control samples measured from the data are found, the data are used to introduce (small) *ad hoc* corrections to the Monte Carlo.

A central point in the unfolding method is the construction of the 'migration matrix' $M_{ij\alpha i'j'\alpha'}$, that is the matrix which describes the distribution of the measurements (p_{m}, θ_{m}, and A_{m}, where A represents the integer PID variable) given a bin in the corresponding physical ('true') variables (p_{p}, θ_{p} and A_{p}). In this analysis the entries in this matrix are obtained with the use of a 'single particle Monte Carlo'. This type of Monte Carlo consists of generating a single particle per event in the target of a given particle type at a given p and θ into the full detector simulation. The effect of this particle measured in the detector is ideally a single particle reconstructed with the same kinematic variables and properly identified. However, all known complications are simulated in the Monte Carlo. In particular, for each of the individual beam momentum settings (corresponding to a period of data taking of about one calendar day) the calibrations of the TPC obtained for these particular runs as well as the characteristics of the incoming beam were used in the Monte Carlo. Especially important is the effect on the efficiency of variations in the map of dead channels.

---

[5]We do not make a correction for the attenuation of the proton beam in the target, so that strictly speaking the cross-sections are valid for a $\lambda_{\text{I}} = 5\%$ target.

The efficiency and the effect of cuts are taken into account by keeping track of the number of generated particles and by entering the measured particle into the migration matrix only when it has been reconstructed. This procedure is equivalent to a multiplicative bin–by–bin efficiency correction. The systematic uncertainty in the efficiency is estimated from the variation observed with the elastic scattering data and the difference of the efficiency observed for the data and the simulation for the protons.

Each point (or bin) in the 3-dimensional phase space (p_p, θ_p and A_p) generates a distribution in the measured variables. The corresponding distributions in the measured variables are then the result of the smearing according to the resolution of the measurements. For this reason the number of bins in the measured variables is larger than in the 'true' variables, in order not to lose the information provided by the resolution of the measurements. The unfolding matrix is obtained using equidistant bins in the true variables. The final binning is then defined taking into account the resolution of the detector and the statistics of the data sample. During this re-binning procedure the full information of the covariance matrix is propagated. The Monte Carlo description of the momentum resolution, although checked with cosmic-ray tracks and elastic scattering data, may not be perfect. Possible discrepancies up to 10% of the resolution are taken into account in the systematic error. The value of the uncertainty is obtained from the analysis of elastic scattering and cosmic-ray data.

Using the unfolding approach, possible known biases in the measurements are taken into account automatically as long as they are described by the Monte Carlo. For example the energy-loss of particles inside the target and material around the inner field cage translate into an average shift of the measured momentum distribution compared to the physical momentum. Known biases are therefore treated in the same way as resolution effects. Uncertainties in the description of the energy-loss and a potential bias in the momentum determination are estimated to be of the order of 3% using the elastic scattering analysis. This variation has been applied in the estimation of the corresponding systematic error.

Also the effects of imperfect PID are treated by representing the distribution of the measured PID of a single particle type over all possible bins in the migration matrix. This procedure allows the background of protons in the pion sample to be subtracted without *a priori* assumptions about the proton spectrum. The effects of a possible difference of the Monte Carlo description of the efficiency and purity of the PID are estimated by varying the cuts differentially for the data and the simulation within the limits estimated with the analysis described in Section 5.5. The performance of the PID is correlated with the momentum and angular measurements, hence the importance of the choice to perform the unfolding simultaneously in these three variables, p, θ and A.

The absorption and decay of particles is simulated by the Monte Carlo. The generated single particle can re-interact and produce background particles by the hadronic or electromagnetic processes. These processes are simulated and can give rise to additional particles reconstructed in the TPC in the same event. In such cases also the additional measurements are entered into the migration matrix. Thus the complete set of observed effects of a single particle generated inside the target are taken into account. Uncertainties in the absorption of secondaries in the material of and close to the IFC of the TPC are taken into account by a variation of 10% of this effect in the simulation. The uncertainty in the production of background due to tertiary particles is larger. A 30% variation of the secondary production was applied. The value of the variation was estimated from a comparison of the results for the cross-sections in the energy regime of this experiment with the predictions of the model used in the simulation. The uncertainty estimate is reasonable since the secondary interactions are in majority produced by protons with a momentum around 1 GeV/c where one expects hadronic models to be more reliable than in the energy range of the present measurements.

A different approach is needed for backgrounds generated by other secondary particles, such as π^0's produced in hadronic interactions of the incident beam particle. The assumption is made that the π^0 spectrum is similar to the spectrum of charged pions. Initial π^- and π^+ spectra are obtained in an analysis without π^0 subtraction. The π^- spectra are then used in the MC for the π^0 distributions. A full simulation of the production and decay into γ's with subsequent conversion in the detector materials is used to predict the background electron and positron tracks. Most of these tracks have a momentum below the threshold for this analysis or low enough to be recognized by dE/dx. The tracks with a PID below the expected value for pions can be rejected as background. In the region below 120 MeV/c a large fraction of the electrons can be unambiguously identified. These tracks are used as relative normalization between data

and MC. The remaining background is then estimated from the distributions of the simulated electron and positron tracks which are accepted as pion tracks with the same criteria as used to select the data. These normalized distributions are subtracted from the data before the unfolding procedure is applied. Uncertainties in the assumption of the π^0 spectrum are taken into account by an alternative assumption that their spectrum follows the average of the π^- and π^+ distribution. An additional systematic error of 10% is assigned to the normalization of the π^0 subtraction using the identified electrons and positrons. At low momenta and small angles the π^0 subtraction introduces the largest systematic uncertainty. It is in principle possible to reject more electrons and positrons by constructing a combined PID estimator based on dE/dx and TOF. To obtain a reliable result, the complete dE/dx and β distributions need to be described including their correlations. In addition, the measurement of the TOF introduces an inefficiency and it has tails coming from background hits. Indeed, such an analysis was performed and gave consistent results. However, its systematic errors are more difficult to estimate.

The absolute normalization of the result is calculated in the first instance relative to the number of incident beam particles accepted by the selection. After unfolding, the factor $\frac{A}{N_A \rho t}$ is applied. Especially at lower momenta, beam particles may miss the target even if their trajectory measured in the MWPCs extrapolates to the target. The effects of such a 'targeting efficiency' were estimated counting secondaries produced in the forward direction and measured in the forward spectrometer as a function of impact radius measured from the centre of the target and found to be smaller than 1%. The measured variation in the target thickness is used as an estimate of an additional uncertainty in the absolute normalization (less than 1%). The target thickness uncertainty cancels in the comparison of data with different incoming beam momenta, while the uncertainty in the efficiency to hit the target introduces an error into this comparison. The beam normalization using down-scaled incident-proton triggers with the same beam particle selection introduces for all settings a statistical uncertainty significantly less than 1% [6]. The combination of above mentioned uncertainties are smaller than 2% for all beam momentum settings.

The background due to interactions of the primary protons outside the target (called 'Empty target background') is measured using data taken without the target mounted in the target holder. Owing to the selection criteria which only accept events from the target region and the good definition of the interaction point this background is negligible ($< 10^{-5}$).

The use of a simulation where only one secondary particle is generated in the target neglects the possible influence of particles on the measurement of the trajectories of each other. Owing to the relatively low multiplicity which is spread over a large solid angle this simplification does not introduce a significant error.

The effects of these uncertainties on the final results are estimated by repeating the analysis with the relevant input modified within the estimated uncertainty intervals. In many cases this procedure requires the construction of a set of different migration matrices. The correlations of the variations between the cross-section bins are evaluated and expressed in the covariance matrix. Each systematic error source is represented by its own covariance matrix. The sum of these matrices describes the total systematic error.

7   Results

Figures 23 and 24 show the measurement of the double-differential cross-section for the production of positively (Fig. 23) and negatively (Fig. 24) charged pions in the laboratory system as a function of the momentum and the polar angle (shown in mrad in the panels) for each incident beam momentum. The error bars represent the combined statistical and systematic error. Correlations cannot be shown in the figures. The errors shown are the square-roots of the diagonal elements in the covariance matrix. Tables with the results of this analysis are also given in Appendix A. A discussion of the error evaluation is given below. The overall scale error (2%) is not shown. The measurements for the different beam momenta are overlaid in the same figure.

The result of the unfolding procedure is the physical cross-section (represented as a histogram) which

---

[6]The statistical error corresponding to down-scaled triggers is smaller than the square-root of the number of collected triggers because the sampling is not random.
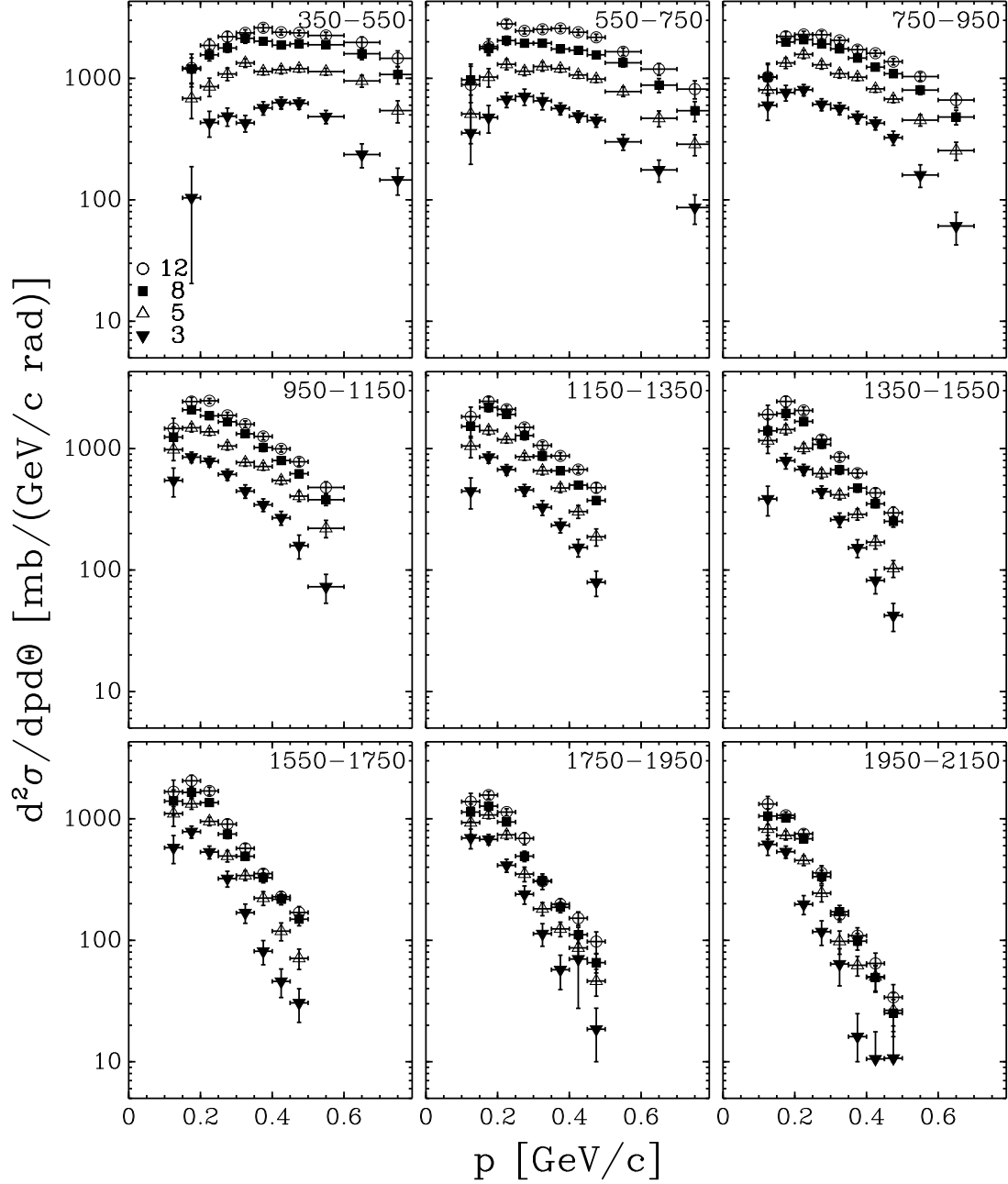
Figure 23: Double-differential cross-sections for π^+ production in p–Ta interactions as a function of momentum displayed in different angular bins (shown in mrad in the panels). The results are given for all incident beam momenta (filled triangles: 3 GeV/c; open triangles: 5 GeV/c; filled rectangles: 8 GeV/c; open circles: 12 GeV/c). The error bars take into account the correlations of the systematic uncertainties.

Figure 24: Double-differential cross-sections for π^- production in p–Ta interactions as a function of momentum displayed in different angular bins (shown in mrad in the panels). The results are given for all incident beam momenta (filled triangles: 3 GeV/c; open triangles: 5 GeV/c; filled rectangles: 8 GeV/c; open circles: 12 GeV/c). The error bars take into account the correlations of the systematic uncertainties.
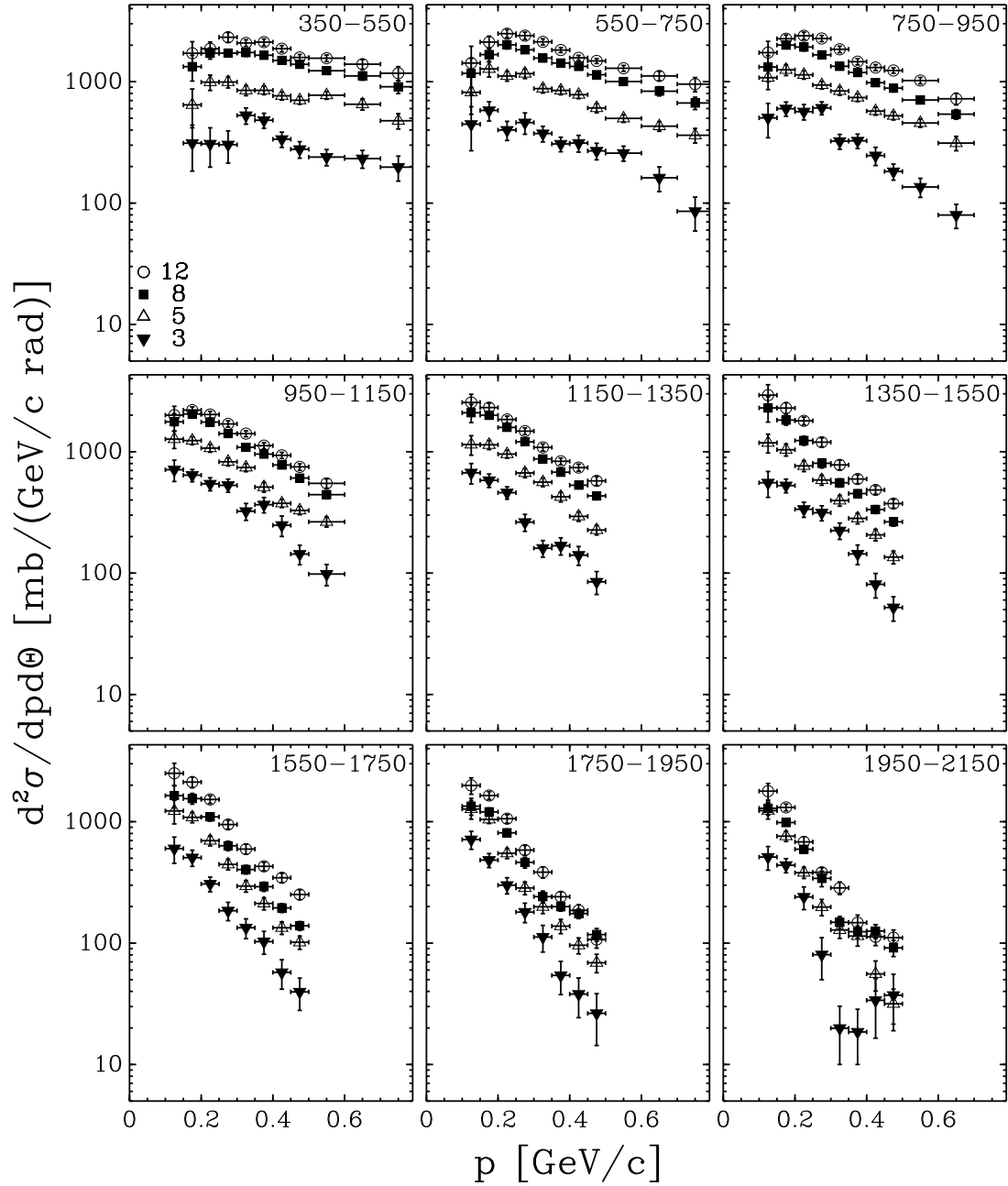
provides the best fit to the measured data, taking into account background, efficiency and resolution. The quality of the fit can be judged from Fig. 25, where the raw data after π^0 subtraction are compared to the description corresponding to the unfolding result for the 8 GeV/c data. This data set has the highest statistics and therefore represents the most stringent test.

To better visualize the dependence on the incoming beam momentum, the same data integrated over the angular range (separately for the forward going and backward going tracks) covered by the analysis are shown separately for π^+ and π^- in Fig. 26. The spectrum of pions produced in the backward direction falls much more steeply than that of the pions produced in the forward direction.

The increase of the pion yield per proton with increasing beam momentum is visible in addition to a change of spectrum. The spectra of the secondaries produced at small angles are harder with increasing beam momentum. Also an asymmetry between π^+ and π^- is observed at relatively small angles with the beam in favour of a higher π^+ rate. At very large angles from the beam the spectra of π^+ and π^- are more symmetric. The integrated π^-/π^+ ratio in the forward direction is displayed in Fig. 27 as a function of secondary momentum. In the largest part of the momentum range more π^+'s are produced than π^-'s, with a smaller π^-/π^+ ratio at lower incoming beam momenta. One observes that the number of π^+'s produced is smaller than the number of π^-'s in the lowest momentum bin (100 MeV/c–150 MeV/c). This effect is only significant at the higher incoming beam momenta. We find a value of 1.52 ± 0.21 and 1.39 ± 0.19 for 12 GeV/c and 8 GeV/c, respectively, and 1.38 ± 0.28 and 1.23 ± 0.17 for 3 GeV/c and 5 GeV/c, respectively. To exclude any detector-related effect one can use the observation that the electrons and positrons in this momentum range are predominantly originating from π^0 decays and subsequent γ conversions. Therefore their number and spectrum must be the same. It was verified that the ratio e^+/e^- was equal to unity within a statistical error of 2%. To increase the sensitivity of this cross-check, data taken with other targets, but within a few days from the tantalum runs reported here, were also used. It was also checked that the ratio of the efficiencies for positive and negative pions predicted by the simulation did not show any unexpected behaviour.

The E910 collaboration makes a similar observation for their lowest momentum bin (100 MeV/c– 140 MeV/c) in p–Au collisions at 12.3 GeV/c and 17.5 GeV/c incoming beam momentum and quotes a π^- to π^+ yield ratio 2–3 [32]. They offer an interesting explanation in the form of Λ^0 production at rest which would enhance the π^- yield at low secondary momenta.

An alternative analysis of the same data using different techniques is described in Appendix B.

7.1   Systematic errors

The uncertainties are reported in some detail in Table 2. To obtain the entries in this table the double-differential cross-sections were integrated in nine regions organized as a three–by–three matrix in angle and momentum. (The ninth bin is not populated.) The angular ranges are 0.35 rad – 0.95 rad, 0.95 rad – 1.55 rad and 1.55 rad – 2.15 rad, two bins in the forward direction and one backward bin. The momentum ranges are 100 MeV/c – 300 MeV/c, 300 MeV/c – 500 MeV/c and 500 MeV/c – 700 MeV/c.

One observes that only for the 3 GeV/c beam is the statistical error similar in magnitude to the systematic error, while the statistical error is negligible for the 8 GeV/c and 12 GeV/c beams. The statistical error is calculated by error propagation as part of the unfolding procedure. It takes into account that the unfolding matrix is obtained from the data themselves and hence contributes also to the statistical error. This procedure almost doubles the statistical error, but avoids an important systematic error which would otherwise be introduced by assuming a cross-section model *a priori* to calculate the corrections.

The largest systematic error corresponds to the uncertainty in the absolute momentum scale, which was estimated to be 3% using elastic scattering (Section 5.2, Fig. 13). It is difficult to better constrain this value, since it depends on the knowledge of the beam momentum (known to 1%) and the measurement of the forward scattering angle in the elastic scattering interaction. At low momentum in the relatively small angle forward direction the uncertainty in the subtraction of the electron and positron background due to π^0 production is dominant. This uncertainty is split between the variation in the shape of the π^0 spectrum and the normalization using the recognized electrons. The target region definition (cuts
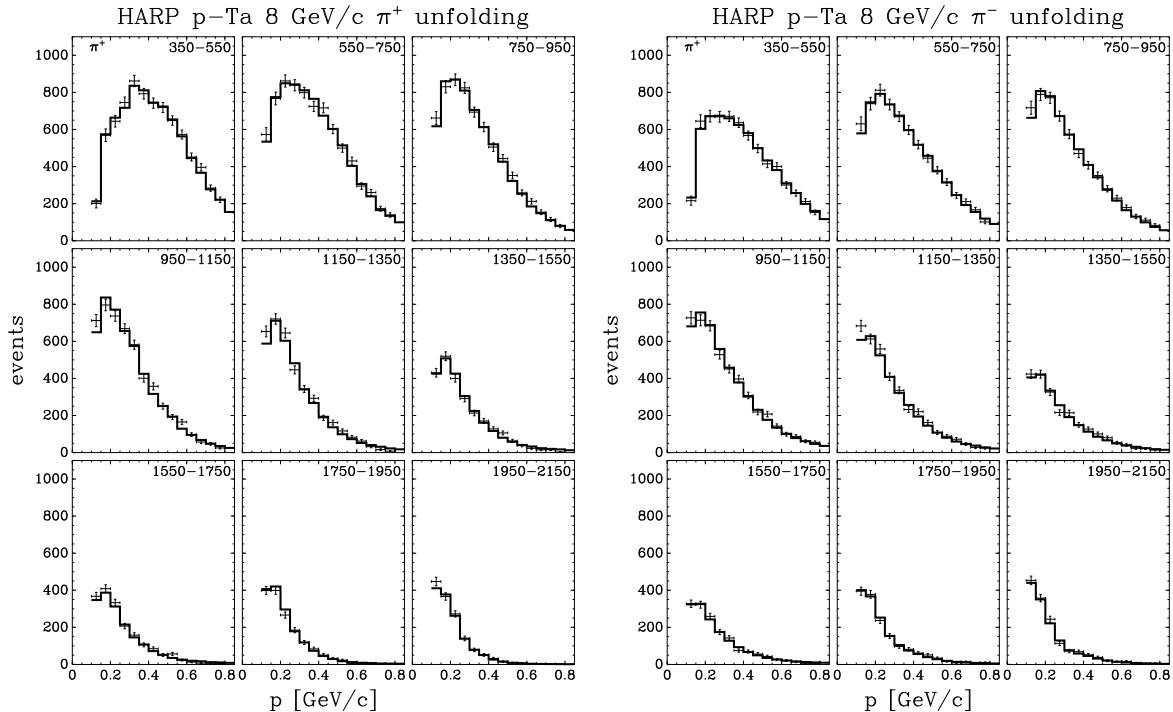
Figure 25: Comparison of the π^0 subtracted raw data in the 8 GeV/c beam (data points) with the prediction in the measured variables corresponding to the result of the unfolding (histogram). Left panel: π^+; right panel: π^-. The error bars represent the statistical error of the background subtracted data. In the unfolding fit a binning twice as fine as shown here is used (both in angle and momentum). For the sake of clarity these bins are summed four-by-four with the appropriate error propagation to obtain the spectra as shown here.

in d_0' and z_0') and the uncertainty in the PID efficiency and background from tertiaries are of similar size and are not negligible. Relatively small errors are introduced by the uncertainties in the absorption correction, absolute knowledge of the angular and the momentum resolution. The correction for tertiaries (particles produced in secondary interactions) is relatively large at low momenta and large angles. The fact that this region is most affected by this component is to be expected.

As already reported above, the overall normalization has an uncertainty of 2%, and is not reported in the table.

8   Comparisons with earlier data

Very few p–Ta pion production data are available in the literature. Our data can only be compared with results from Ref. [33] where measurements of π^- production are reported in 10 GeV/c p–Ta interactions. The total number of π^- observed in the above reference is about 2600. No relevant π^+ production data were found in the literature. In the paper cited above no table of the double differential cross-sections was provided, the measurements being given in parametrized and graphical form only. The authors of Ref. [33] give the results as a simple exponential in the invariant cross-section: $\frac{E}{A}\frac{\mathrm{d}^3\sigma}{\mathrm{d}p^3}$, where E and p are the energy and momentum of the produced particle, respectively, and A the atomic number of the target nucleus. They parametrize their spectra in each angular bin with a function of the form $f_{\pi^-} = c \, \exp\left(-T/T_0\right)$, where T is the kinetic energy of the produced particle and T_0 is given by $T_0 = T'/(1 - \beta \, \cos\theta)$. The values of the parameters are $T' = (0.086 \pm 0.006)$ GeV/c and $\beta = 0.78 \pm 0.03$. Unfortunately, no absolute normalization is given numerically. To provide a comparison with these data, the parametrization was integrated over the angular bins used in our analysis and with an arbitrary overall normalization overlaid over our 8 GeV/c and 12 GeV/c results. The results of this comparison are shown in Fig. 28. The shaded
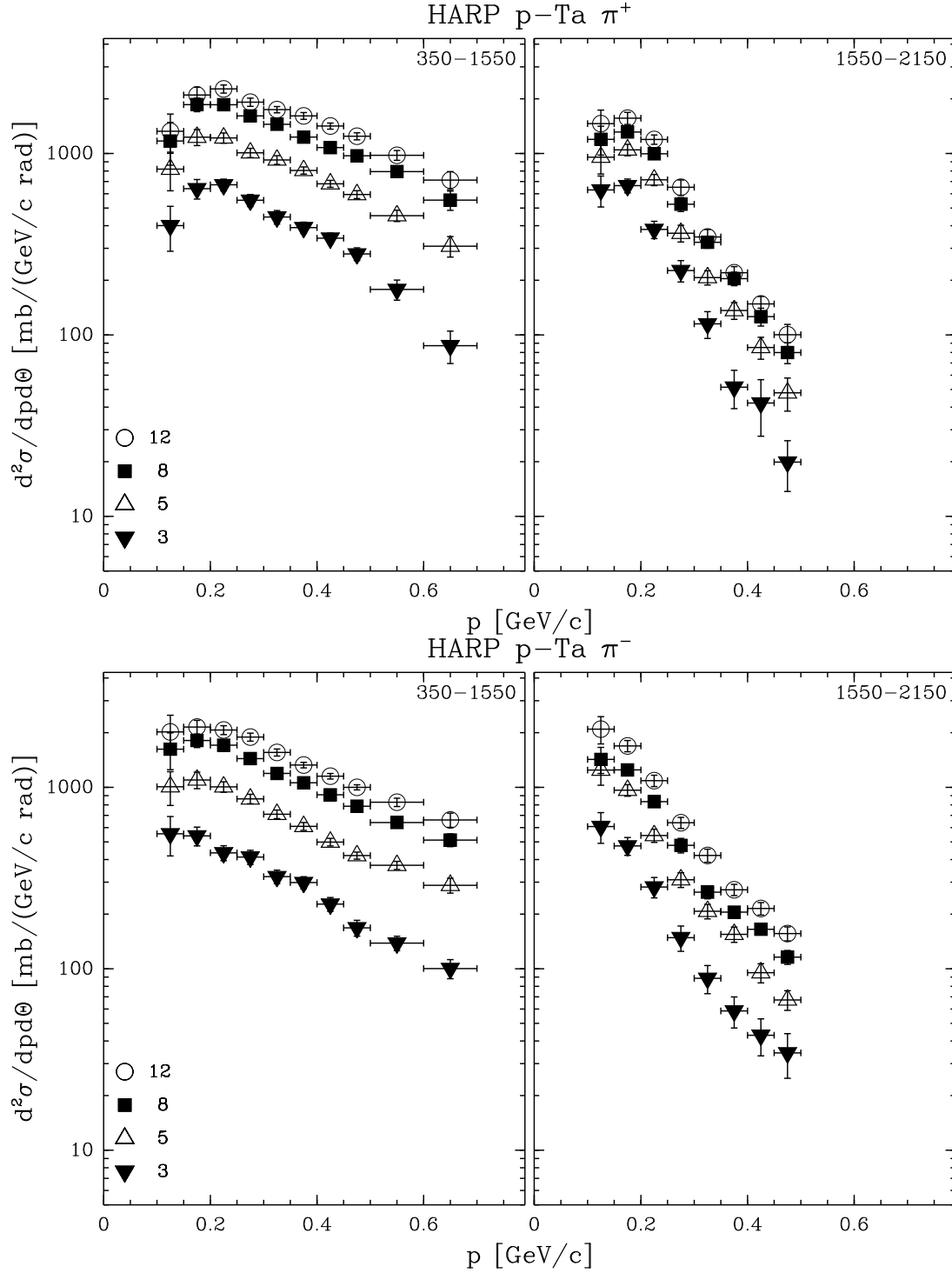
Figure 26: Double-differential cross-sections for π^+ (top panel) and π^- (bottom panel) production in p–Ta interactions as a function of momentum averaged over the angular region covered by this experiment (shown in mrad). Left: forward production (350 mrad $\leq \theta <$ 1550 mrad); Right: backward production (1550 mrad $\leq \theta <$ 2150 mrad). The results are given for all incident beam momenta (filled triangles: 3 GeV/c; open triangles: 5 GeV/c; filled rectangles: 8 GeV/c; open circles: 12 GeV/c).

36

Table 2: Contributions to the experimental uncertainties. The numbers represent the uncertainty in percent of the cross-section integrated over the angle and momentum region indicated.

| Momentum range (MeV/c)	100 − 300			300 − 500			500 − 700	
Angle range (rad)	0.35–	0.95–	1.55–	0.35–	0.95–	1.55–	0.35–	0.95–
Error source	0.95	1.55	2.15	0.95	1.55	2.15	0.95	1.55
3 GeV/c beam								
Absorption	1.3	1.8	2.4	0.6	0.5	0.3	0.3	0.5
Tertiaries	3.1	4.4	5.0	2.5	2.9	1.8	0.1	0.6
Target region cut	3.2	1.0	1.1	2.1	0.6	2.8	0.8	2.0
Efficiency	1.7	1.9	1.3	2.1	2.8	2.2	2.6	2.8
Shape of π^0	8.6	1.9	0.0	0.1	0.0	0.1	0.0	0.0
Normalization of π^0	5.5	1.9	0.9	0.2	0.1	0.0	0.0	0.0
Particle ID	0.1	0.1	0.0	1.1	0.5	0.0	5.5	3.5
Momentum resolution	2.7	1.5	1.6	0.5	0.1	0.6	0.4	0.3
Momentum scale	7.0	4.4	3.6	1.2	4.0	4.4	7.0	11.3
Angle bias	1.5	0.8	0.4	0.2	1.3	0.9	1.0	1.5
Total systematics	13.7	7.5	7.1	4.2	5.9	6.0	9.4	12.5
Statistics	5.0	3.9	4.9	3.9	5.3	10.6	5.4	10.2
5 GeV/c beam								
Absorption	1.2	1.9	2.4	0.6	0.5	0.4	0.3	0.4
Tertiaries	3.0	4.4	5.0	2.6	2.8	2.0	0.2	0.1
Target region cut	2.8	0.9	1.2	1.0	0.6	0.6	0.1	0.2
Efficiency	1.7	2.2	1.5	1.6	2.4	2.3	1.7	2.9
Shape of π^0	6.9	0.6	0.6	0.2	0.1	0.1	0.0	0.0
Normalization of π^0	6.0	2.1	1.0	0.2	0.1	0.0	0.0	0.0
Particle ID	0.1	0.1	0.0	1.0	0.5	0.1	5.0	4.0
Momentum resolution	2.3	1.9	1.8	0.1	0.6	0.9	0.3	0.9
Momentum scale	6.1	4.8	4.1	1.3	2.6	5.5	4.2	9.7
Angle bias	0.9	0.7	0.4	0.2	1.2	0.6	0.8	2.0
Total systematics	12.2	7.7	7.5	3.6	4.8	6.4	6.8	11.1
Statistics	2.7	2.2	2.7	2.0	2.7	4.9	2.4	4.2
8 GeV/c beam								
Absorption	1.3	1.9	2.2	0.6	0.6	0.4	0.3	0.5
Tertiaries	2.5	4.4	4.2	2.6	3.3	2.1	0.2	0.3
Target region cut	3.1	2.2	1.2	2.3	0.4	1.1	1.6	0.6
Efficiency	1.4	1.9	1.4	1.3	2.1	1.9	1.5	2.5
Shape of π^0	4.0	0.3	0.4	0.1	0.1	0.1	0.0	0.0
Normalization of π^0	6.3	2.0	1.1	0.2	0.1	0.0	0.0	0.0
Particle ID	0.1	0.1	0.0	1.3	0.6	0.2	5.5	3.6
Momentum resolution	2.3	2.2	1.9	0.0	0.2	0.4	0.0	0.2
Momentum scale	6.4	5.2	4.4	1.3	2.0	4.5	3.9	9.3
Angle bias	0.7	0.6	0.3	0.4	1.2	0.7	1.0	1.1
Total systematics	11.1	8.3	7.1	4.2	4.6	5.5	7.2	10.4
Statistics	1.6	1.4	1.8	1.2	1.6	2.9	1.4	2.3
12 GeV/c beam								
Absorption	1.1	1.8	2.1	0.5	0.5	0.5	0.3	0.3
Tertiaries	0.8	3.5	4.3	0.8	2.5	1.8	1.3	0.0
Target region cut	3.8	2.3	1.0	2.3	0.6	0.2	1.1	0.2
Efficiency	1.6	2.3	2.5	1.1	2.4	2.3	1.2	2.4
Shape of π^0	4.4	0.5	1.2	0.1	0.1	0.1	0.0	0.0
Normalization of π^0	6.5	2.2	1.1	0.4	0.1	0.1	0.1	0.0
Particle ID	0.0	0.0	0.0	1.1	0.5	0.0	5.3	3.8
Momentum resolution	2.2	2.3	2.4	0.2	1.0	0.4	0.1	0.8
Momentum scale	7.3	5.2	4.7	1.1	1.7	4.9	3.7	10.0
Angle bias	0.5	0.6	0.1	0.5	1.1	0.7	0.9	1.8
Total systematics	11.8	8.0	7.8	3.2	4.2	5.8	6.8	11.1
Statistics	1.7	1.6	2.0	1.3	1.8	3.3	1.5	2.6
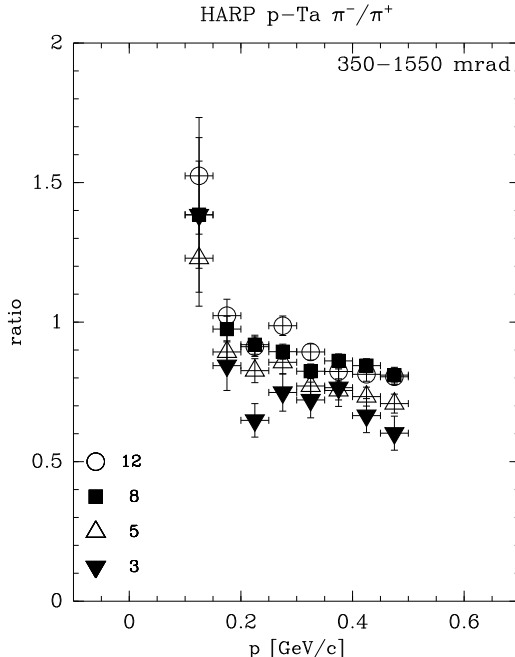
Figure 27: The ratio of the differential cross-sections for π^- and π^+ production in p–Ta interactions as a function of momentum integrated over the forward angular region (shown in mrad). The results are given for all incident beam momenta (filled triangles: 3 GeV/c; open triangles: 5 GeV/c; filled rectangles: 8 GeV/c; open circles: 12 GeV/c).

band gives the excursion of the parametrization due to the error in the slope parameters ($\pm 2\sigma$) with an additional assumed 10% error on the absolute scale. The latter additional error takes into account the fact that the errors on the slopes fitted to the individual angular bins in the cited data are at least a factor of two larger than in the exponential slope obtained from their global parametrization. The agreement of our data with the simple parametrization is good. Since the comparison is of similar quality for the two incoming beam momenta, the lack of data with an exactly equal beam momentum does not play a role. To judge the comparison, one should keep in mind that the statistics of Ref. [33] is much smaller (2600 π^-) than the statistics of the π^- samples in our 8 GeV/c and 12 GeV/c data (38,000 and 29,000 π^-, respectively). The bands in the figure extend over the region where there is data available from Ref. [33].

9   Implications for neutrino factory designs

The data presented in this paper are particularly relevant for the design of the input stage of future neutrino factories. In addition, they will be valuable in validating and possibly improving hadronic production models in a kinematic region where data are scarce. The kinematic coverage of the experiment is compared with the typical range of the kinematical acceptance of neutrino factory designs in Fig. 29. It is shown that this experiment covers the full momentum range of interest for production angles above 0.35 rad. A small part of the small angle region can in principle be covered by measurements with the HARP forward spectrometer. The analysis of the p–Ta data in the forward direction is in progress. The analysis reported here covers the major part of pions produced in the target and accepted by the focusing system of the input stage of a neutrino factory. The importance of the knowledge of the smaller angles varies with the different types of design being contemplated. The effective coverage of the kinematic range can be defined as the fraction of the number of muons transported by the input stage of a neutrino factory design originating from decays for which the pion production cross-section is within the kinematic range measured by the present experiment. As an example, this effective coverage was evaluated for the ISS input stage [34] to be 69% for π^+ and 72% for π^-, respectively [35], using a particular model for pion production at an incoming beam momentum of 10.9 GeV/c [36].
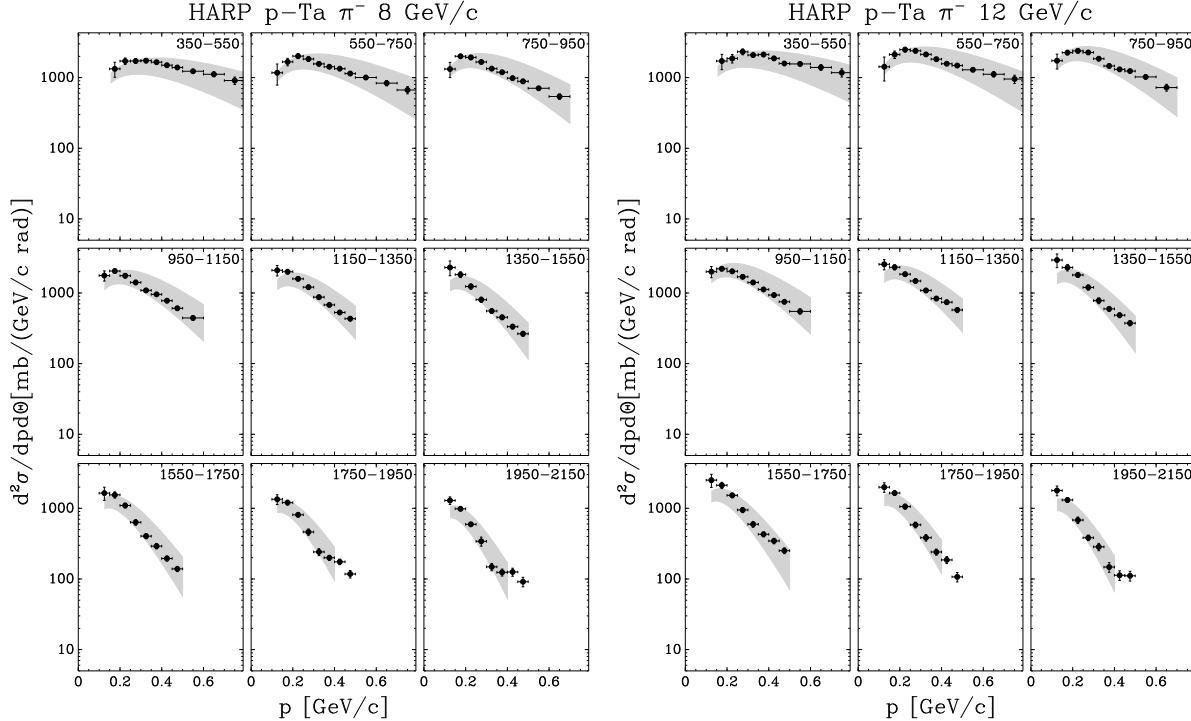
Figure 28: Comparison of the HARP data with data from Ref. [33]. The left panel shows the comparison of the parametrization of the 10 GeV/c data of Ref. [33] with the 8 GeV/c data reported here; the right panel shows the comparison with the 12 GeV/c data. The absolute normalization of the parametrization was fixed to the data in both cases. The band shows the range allowed by varying the slope parameters given by [33] with two standard deviation and a 10% variation on the absolute scale.

There are a number of options to obtain pion production rates for the angular range below 0.35 rad. One option is to adjust hadron production models to the available data and to use the extrapolation of these models in the unmeasured region. Such tuning of models can also profit from the additional data provided with the forward spectrometer. In principle, the combination of the particle tracking in the large angle and forward spectrometer can be developed and the region can be extended towards angles near to the beam direction. In that case the limits are given by the requirement $p_T > 50$ MeV/c and by the minimum angle to remove through-going beam particles (≈ 30 mrad).

As an indication of the overall pion yield as a function of incoming beam momentum, the π^+ and π^- production cross-sections were integrated over the full HARP kinematic range in the forward hemisphere (100 MeV/$c < p < 700$ MeV/c and $0.35 < \theta < 1.55$). The results are shown in Fig. 30[7]. The integrated yields are shown in the left panel and the integrated yields normalized to the kinetic energy of the incoming beam particles are shown in the right panel. The outer error bars indicate the total statistical and systematic errors. If one compares the π^+ and π^- rates for a given beam momentum or if one compares the rates at a different beam momentum the relative systematic error is reduced by about a factor two. The relative uncertainties are shown as inner error bar. It is shown that the pion yield increases with momentum and that in our kinematic coverage the optimum yield is between 5 GeV/c and 8 GeV/c. However, these calculations should be completed with more realistic kinematical cuts in the integration. To show the trend the rates within restricted ranges are also given: a restricted angular range ($0.35 < \theta < 0.95$) and a range further restricted in momentum (250 MeV/$c < p < 500$ MeV/c). The latter range may be most representative for the neutrino factory.

Of course this analysis only gives a simplified picture of the results. One should note that the best result can be obtained by using the full information of the double-differential cross-section and by developing

---

[7] Although the units are indicated as "arbitrary", for the largest region, the yield is expressed as $\mathrm{d}^2\sigma/\mathrm{d}p\mathrm{d}\Omega$ in mb/(GeV/c sr). For the other regions the same normalization is chosen, but now scaled with the relative bin size to show visually the correct ratio of number of pions produced in these kinematic regions.
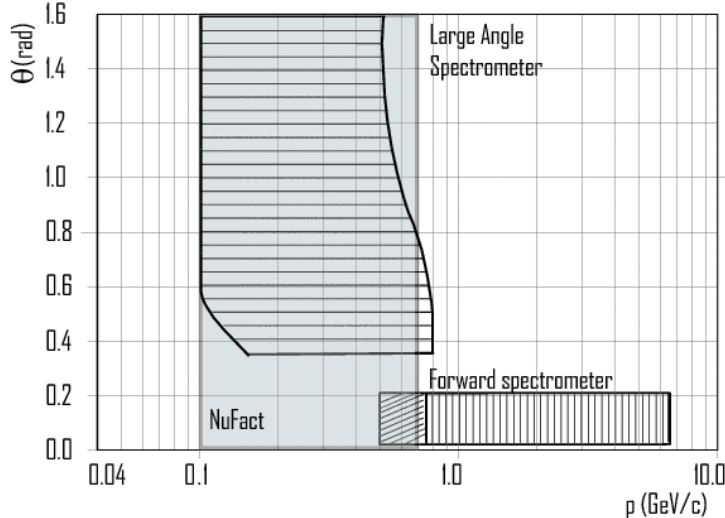
Figure 29: Kinematic region in the p–θ plane covered by this analysis compared to the maximum acceptance of an input stage of typical neutrino factory designs. The different neutrino factory designs have in addition to the limits shown different limits in p_T.

designs optimized specifically for each single beam momentum. Then these optimized designs can be compared.

10 Summary and Conclusions

In this paper an analysis of the production of pions at large angles with respect to the beam direction for protons of 3 GeV/c, 5 GeV/c, 8 GeV/c and 12 GeV/c impinging on a thin (5% λ_I) tantalum target was described. The secondary pion yield was measured in a large angular and momentum range and double-differential cross-sections were obtained. A detailed error estimation has been discussed.

The use of a single detector for a range of beam momenta makes it possible to measure the dependence of the pion yield on the beam momentum with high precision. These data can be used to make predictions for the fluxes of pions to enable an optimized design of a future neutrino factory.

Very few pion production measurements in this energy range are reported in the literature. The only comparable data found in the literature agrees with the results described in this paper. Hadronic production models describing this energy range can now be compared with the new results and, if needed, improved. Data have been taken with different target materials (Be, C, Al, Cu, Sn and Pb) for the beam momenta 3 GeV/c, 5 GeV/c, 8 GeV/c, 12 GeV/c and 15 GeV/c and will be presented in subsequent papers. In particular, the data taken with a lead target will add valuable information to the studies for the neutrino factory. Also data with thick (one λ_I) Ta and Pb targets have been taken which would help modelling the neutrino factory yields.

11 Acknowledgements
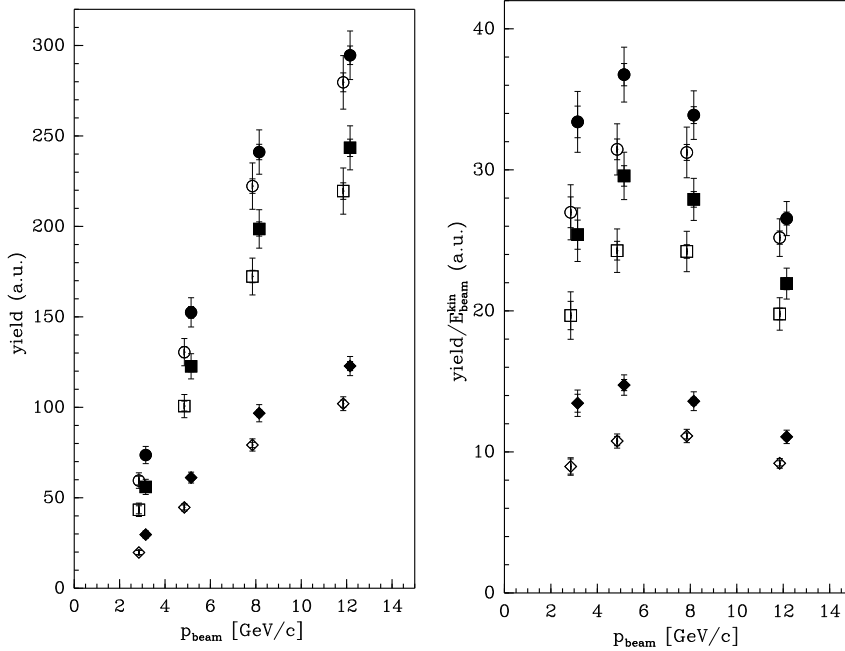
Figure 30: Prediction of the π^+ (closed symbols) and π^- (open symbols) yield as a function of incident proton beam momentum for different designs of the neutrino factory focusing stage. Shown are the integrated yields (left) and the integrated yields normalized to the kinetic energy of the proton (right). The circles indicate the integral over the full HARP acceptance, the squares are integrated over 0.35 rad < θ < 0.95 rad, while the diamonds are calculated for the restricted angular range and 250 MeV/c < p < 500 MeV/c. The full error bar shows the overall (systematic and statistical) error, while the inner error bar shows the error relevant for the point–to-point comparison. For the latter error only the uncorrelated systematic uncertainties were added to the statistical error.

A Cross-section data

Table 3: HARP results for the double-differential π^+ production cross-section in the laboratory system, $d^2\sigma^{\pi^+}/(dpd\theta)$. Each row refers to a different $(p_{\min} \leq p < p_{\max}, \theta_{\min} \leq \theta < \theta_{\max})$ bin, where p and θ are the pion momentum and polar angle, respectively. The central value as well as the square-root of the diagonal elements of the covariance matrix are given.

$\theta_{\min}$ (rad)	$\theta_{\max}$ (rad)	$p_{\min}$ (GeV/c)	$p_{\max}$ (GeV/c)	$d^2\sigma^{\pi^+}/(dpd\theta)$ (barn/(GeV/c rad))			
				3 GeV/**c**	**5** GeV/**c**	**8** GeV/**c**	**12** GeV/**c**
0.35	0.55	0.15	0.20	0.10±0.08	0.68±0.22	1.19±0.28	1.22±0.37
		0.20	0.25	0.43±0.10	0.86±0.15	1.56±0.17	1.87±0.24
		0.25	0.30	0.49±0.08	1.09±0.13	1.78±0.15	2.20±0.22
		0.30	0.35	0.43±0.07	1.34±0.11	2.14±0.19	2.37±0.14
		0.35	0.40	0.57±0.07	1.14±0.07	2.02±0.12	2.61±0.18
		0.40	0.45	0.63±0.07	1.18±0.09	1.88±0.12	2.39±0.12
		0.45	0.50	0.62±0.07	1.20±0.08	1.93±0.15	2.37±0.12
		0.50	0.60	0.48±0.06	1.14±0.07	1.89±0.12	2.25±0.14
		0.60	0.70	0.24±0.05	0.95±0.11	1.60±0.17	1.98±0.21
		0.70	0.80	0.15±0.04	0.54±0.11	1.08±0.18	1.46±0.22
0.55	0.75	0.10	0.15	0.35±0.16	0.51±0.22	0.97±0.34	0.89±0.37
		0.15	0.20	0.48±0.12	1.02±0.18	1.76±0.18	1.83±0.29
		0.20	0.25	0.67±0.09	1.31±0.13	2.05±0.17	2.80±0.22
		0.25	0.30	0.71±0.11	1.14±0.09	1.94±0.11	2.46±0.14
		0.30	0.35	0.65±0.10	1.25±0.11	1.95±0.12	2.54±0.16
		0.35	0.40	0.56±0.06	1.20±0.08	1.75±0.12	2.58±0.15
		0.40	0.45	0.49±0.05	1.07±0.07	1.70±0.10	2.39±0.14
		0.45	0.50	0.45±0.05	0.99±0.07	1.56±0.09	2.17±0.13
		0.50	0.60	0.30±0.04	0.78±0.07	1.34±0.11	1.66±0.12
		0.60	0.70	0.18±0.04	0.47±0.07	0.88±0.12	1.19±0.13
		0.70	0.80	0.086±0.023	0.29±0.06	0.54±0.10	0.82±0.14
0.75	0.95	0.10	0.15	0.60±0.15	0.80±0.19	1.02±0.27	1.03±0.30
		0.15	0.20	0.76±0.11	1.34±0.13	1.99±0.14	2.22±0.21
		0.20	0.25	0.80±0.09	1.58±0.13	2.08±0.11	2.30±0.14
		0.25	0.30	0.61±0.07	1.29±0.10	1.92±0.11	2.28±0.17
		0.30	0.35	0.57±0.06	1.09±0.09	1.75±0.09	2.05±0.12
		0.35	0.40	0.48±0.06	1.02±0.07	1.47±0.08	1.72±0.12
		0.40	0.45	0.43±0.05	0.82±0.05	1.24±0.08	1.61±0.09
		0.45	0.50	0.32±0.04	0.68±0.05	1.09±0.06	1.37±0.08
		0.50	0.60	0.160±0.034	0.45±0.05	0.80±0.07	1.03±0.08
		0.60	0.70	0.061±0.018	0.25±0.04	0.48±0.07	0.66±0.09
0.95	1.15	0.10	0.15	0.55±0.14	0.98±0.19	1.24±0.26	1.46±0.31
		0.15	0.20	0.85±0.08	1.49±0.11	2.08±0.14	2.44±0.20
		0.20	0.25	0.78±0.08	1.37±0.09	1.86±0.12	2.47±0.12
		0.25	0.30	0.61±0.06	1.05±0.08	1.66±0.10	1.88±0.11
		0.30	0.35	0.45±0.06	0.77±0.05	1.32±0.08	1.59±0.10
		0.35	0.40	0.34±0.04	0.71±0.05	1.02±0.07	1.26±0.08
		0.40	0.45	0.27±0.04	0.55±0.04	0.80±0.05	0.99±0.06
		0.45	0.50	0.16±0.04	0.41±0.04	0.62±0.04	0.78±0.06
		0.50	0.60	0.073±0.019	0.22±0.04	0.38±0.04	0.48±0.05

$\theta_{\min}$ (rad)	$\theta_{\max}$ (rad)	$p_{\min}$ (GeV/c)	$p_{\max}$ (GeV/c)	$d^2\sigma^{\pi^+}/(dpd\theta)$ (barn/(GeV/c rad))			
				3 GeV/**c**	**5** GeV/**c**	**8** GeV/**c**	**12** GeV/**c**
1.15	1.35	0.10	0.15	0.45±0.13	1.05±0.21	1.52±0.30	1.83±0.36
		0.15	0.20	0.85±0.09	1.41±0.12	2.18±0.17	2.45±0.21
		0.20	0.25	0.67±0.07	1.19±0.08	1.91±0.11	2.11±0.15
		0.25	0.30	0.46±0.05	0.86±0.06	1.28±0.10	1.49±0.10
		0.30	0.35	0.33±0.05	0.66±0.05	0.87±0.06	1.06±0.08
		0.35	0.40	0.233±0.031	0.47±0.04	0.66±0.04	0.87±0.05
		0.40	0.45	0.153±0.025	0.30±0.04	0.501±0.032	0.67±0.04
		0.45	0.50	0.079±0.019	0.188±0.030	0.374±0.027	0.48±0.04
1.35	1.55	0.10	0.15	0.38±0.11	1.16±0.25	1.40±0.36	1.90±0.37
		0.15	0.20	0.79±0.11	1.43±0.14	1.94±0.22	2.44±0.26
		0.20	0.25	0.67±0.07	1.01±0.10	1.67±0.12	2.06±0.14
		0.25	0.30	0.44±0.05	0.62±0.06	1.08±0.08	1.19±0.09
		0.30	0.35	0.26±0.04	0.42±0.04	0.67±0.05	0.85±0.06
		0.35	0.40	0.152±0.025	0.288±0.030	0.47±0.04	0.63±0.05
		0.40	0.45	0.082±0.018	0.170±0.021	0.351±0.024	0.43±0.04
		0.45	0.50	0.042±0.011	0.103±0.016	0.252±0.026	0.30±0.04
1.55	1.75	0.10	0.15	0.58±0.15	1.11±0.24	1.40±0.33	1.67±0.41
		0.15	0.20	0.78±0.09	1.33±0.14	1.65±0.17	2.06±0.23
		0.20	0.25	0.53±0.06	0.95±0.08	1.36±0.09	1.69±0.13
		0.25	0.30	0.32±0.05	0.49±0.05	0.75±0.06	0.90±0.09
		0.30	0.35	0.168±0.030	0.341±0.032	0.49±0.04	0.57±0.05
		0.35	0.40	0.081±0.018	0.222±0.029	0.327±0.030	0.353±0.031
		0.40	0.45	0.046±0.012	0.119±0.020	0.218±0.022	0.228±0.023
		0.45	0.50	0.030±0.009	0.071±0.014	0.149±0.018	0.169±0.020
1.75	1.95	0.10	0.15	0.69±0.13	0.93±0.19	1.14±0.19	1.39±0.23
		0.15	0.20	0.68±0.07	1.08±0.08	1.27±0.09	1.57±0.11
		0.20	0.25	0.41±0.05	0.74±0.06	0.94±0.06	1.14±0.08
		0.25	0.30	0.24±0.04	0.35±0.05	0.49±0.05	0.69±0.08
		0.30	0.35	0.113±0.024	0.182±0.023	0.309±0.027	0.31±0.05
		0.35	0.40	0.057±0.018	0.124±0.017	0.187±0.019	0.198±0.022
		0.40	0.45	0.07±0.04	0.087±0.015	0.111±0.017	0.152±0.019
		0.45	0.50	0.019±0.009	0.046±0.012	0.065±0.012	0.098±0.020
1.95	2.15	0.10	0.15	0.61±0.12	0.82±0.14	1.05±0.16	1.33±0.20
		0.15	0.20	0.53±0.06	0.73±0.06	1.02±0.05	1.07±0.07
		0.20	0.25	0.20±0.04	0.45±0.04	0.69±0.05	0.75±0.06
		0.25	0.30	0.118±0.027	0.24±0.04	0.33±0.04	0.36±0.05
		0.30	0.35	0.064±0.022	0.098±0.021	0.172±0.022	0.162±0.021
		0.35	0.40	0.016±0.009	0.062±0.011	0.098±0.015	0.109±0.018
		0.40	0.45	0.011±0.007	0.050±0.012	0.049±0.012	0.064±0.014
		0.45	0.50	0.011±0.009	0.027±0.010	0.025±0.007	0.034±0.009

Table 4: HARP results for the double-differential π^- production cross-section in the laboratory system, $d^2\sigma^{\pi^-}/(dpd\theta)$. Each row refers to a different $(p_{\min} \leq p < p_{\max}, \theta_{\min} \leq \theta < \theta_{\max})$ bin, where p and θ are the pion momentum and polar angle, respectively. The central value as well as the square-root of the diagonal elements of the covariance matrix are given.

$\theta_{\min}$ (rad)	$\theta_{\max}$ (rad)	$p_{\min}$ (GeV/c)	$p_{\max}$ (GeV/c)	$d^2\sigma^{\pi^-}/(dpd\theta)$ (barn/(GeV/c rad))			
				3 GeV/**c**	**5** GeV/**c**	**8** GeV/**c**	**12** GeV/**c**
0.35	0.55	0.15	0.20	0.31±0.13	0.64±0.23	1.33±0.32	1.71±0.42
		0.20	0.25	0.31±0.11	0.99±0.14	1.71±0.18	1.87±0.26
		0.25	0.30	0.30±0.09	0.99±0.11	1.72±0.12	2.32±0.22
		0.30	0.35	0.53±0.08	0.85±0.08	1.74±0.13	2.08±0.14
		0.35	0.40	0.48±0.07	0.85±0.07	1.65±0.10	2.12±0.14
		0.40	0.45	0.34±0.05	0.76±0.06	1.50±0.08	1.87±0.11
		0.45	0.50	0.28±0.04	0.70±0.05	1.39±0.07	1.58±0.09
		0.50	0.60	0.24±0.04	0.77±0.06	1.23±0.07	1.56±0.10
		0.60	0.70	0.23±0.04	0.65±0.07	1.12±0.09	1.39±0.13
		0.70	0.80	0.20±0.05	0.48±0.07	0.91±0.11	1.18±0.16
0.55	0.75	0.10	0.15	0.45±0.18	0.82±0.28	1.17±0.39	1.43±0.53
		0.15	0.20	0.58±0.10	1.28±0.18	1.67±0.20	2.12±0.25
		0.20	0.25	0.40±0.07	1.11±0.10	2.02±0.16	2.49±0.19
		0.25	0.30	0.46±0.09	1.17±0.10	1.83±0.12	2.39±0.17
		0.30	0.35	0.37±0.06	0.88±0.07	1.56±0.10	2.13±0.13
		0.35	0.40	0.31±0.04	0.85±0.07	1.43±0.08	1.82±0.09
		0.40	0.45	0.31±0.05	0.78±0.06	1.34±0.07	1.57±0.08
		0.45	0.50	0.27±0.04	0.61±0.05	1.14±0.06	1.48±0.07
		0.50	0.60	0.26±0.04	0.50±0.04	1.00±0.05	1.29±0.07
		0.60	0.70	0.16±0.04	0.43±0.04	0.84±0.07	1.12±0.10
		0.70	0.80	0.086±0.027	0.36±0.05	0.67±0.08	0.96±0.13
0.75	0.95	0.10	0.15	0.50±0.16	1.08±0.22	1.32±0.32	1.74±0.41
		0.15	0.20	0.60±0.08	1.25±0.13	2.00±0.13	2.26±0.16
		0.20	0.25	0.57±0.08	1.14±0.09	1.93±0.13	2.39±0.17
		0.25	0.30	0.61±0.07	0.94±0.07	1.67±0.09	2.27±0.13
		0.30	0.35	0.32±0.05	0.84±0.07	1.34±0.07	1.85±0.11
		0.35	0.40	0.33±0.04	0.74±0.05	1.19±0.06	1.46±0.09
		0.40	0.45	0.25±0.04	0.57±0.04	0.98±0.06	1.31±0.07
		0.45	0.50	0.182±0.028	0.52±0.04	0.88±0.06	1.24±0.06
		0.50	0.60	0.136±0.024	0.46±0.04	0.71±0.04	1.02±0.06
		0.60	0.70	0.080±0.018	0.31±0.04	0.54±0.05	0.72±0.08
0.95	1.15	0.10	0.15	0.71±0.14	1.27±0.21	1.76±0.29	2.00±0.36
		0.15	0.20	0.64±0.07	1.23±0.09	2.04±0.14	2.20±0.14
		0.20	0.25	0.54±0.07	1.07±0.08	1.75±0.13	2.02±0.13
		0.25	0.30	0.53±0.07	0.83±0.06	1.41±0.10	1.69±0.10
		0.30	0.35	0.32±0.05	0.74±0.06	1.09±0.07	1.41±0.08
		0.35	0.40	0.37±0.05	0.51±0.05	0.96±0.05	1.12±0.06
		0.40	0.45	0.25±0.05	0.376±0.029	0.78±0.05	0.93±0.06
		0.45	0.50	0.143±0.026	0.328±0.026	0.61±0.04	0.75±0.05
		0.50	0.60	0.098±0.019	0.264±0.025	0.443±0.033	0.55±0.05

$\theta_{\min}$ (rad)	$\theta_{\max}$ (rad)	$p_{\min}$ (GeV/c)	$p_{\max}$ (GeV/c)	$d^2\sigma^{\pi^-}/(dpd\theta)$ (barn/(GeV/c rad))			
				3 GeV/c	**5 GeV/c**	**8 GeV/c**	**12 GeV/c**
1.15	1.35	0.10	0.15	0.67±0.13	1.15±0.21	2.09±0.36	2.55±0.43
		0.15	0.20	0.58±0.07	1.14±0.10	2.00±0.14	2.31±0.19
		0.20	0.25	0.46±0.05	0.96±0.07	1.59±0.10	1.84±0.12
		0.25	0.30	0.26±0.04	0.67±0.06	1.21±0.08	1.48±0.09
		0.30	0.35	0.160±0.025	0.56±0.05	0.87±0.06	1.09±0.07
		0.35	0.40	0.168±0.027	0.42±0.04	0.68±0.04	0.83±0.05
		0.40	0.45	0.141±0.025	0.293±0.026	0.530±0.031	0.74±0.05
		0.45	0.50	0.085±0.018	0.227±0.021	0.432±0.030	0.57±0.05
1.35	1.55	0.10	0.15	0.55±0.13	1.18±0.21	2.29±0.54	2.92±0.64
		0.15	0.20	0.53±0.07	1.04±0.12	1.82±0.17	2.29±0.24
		0.20	0.25	0.34±0.05	0.76±0.08	1.24±0.11	1.79±0.13
		0.25	0.30	0.31±0.04	0.58±0.06	0.80±0.07	1.20±0.10
		0.30	0.35	0.224±0.035	0.40±0.04	0.55±0.04	0.78±0.07
		0.35	0.40	0.144±0.026	0.282±0.028	0.452±0.033	0.60±0.05
		0.40	0.45	0.081±0.019	0.206±0.022	0.334±0.025	0.48±0.04
		0.45	0.50	0.052±0.012	0.135±0.016	0.265±0.021	0.373±0.031
1.55	1.75	0.10	0.15	0.60±0.15	1.23±0.27	1.64±0.35	2.50±0.53
		0.15	0.20	0.51±0.08	1.09±0.11	1.55±0.16	2.12±0.22
		0.20	0.25	0.31±0.04	0.70±0.07	1.10±0.08	1.52±0.11
		0.25	0.30	0.185±0.032	0.45±0.05	0.63±0.06	0.95±0.08
		0.30	0.35	0.134±0.025	0.295±0.032	0.403±0.033	0.59±0.06
		0.35	0.40	0.103±0.022	0.212±0.024	0.292±0.025	0.429±0.033
		0.40	0.45	0.057±0.016	0.134±0.016	0.195±0.016	0.345±0.031
		0.45	0.50	0.040±0.012	0.101±0.013	0.139±0.012	0.251±0.023
1.75	1.95	0.10	0.15	0.71±0.12	1.27±0.22	1.34±0.21	1.99±0.31
		0.15	0.20	0.48±0.06	1.04±0.08	1.20±0.09	1.64±0.12
		0.20	0.25	0.30±0.05	0.55±0.05	0.81±0.06	1.06±0.09
		0.25	0.30	0.180±0.033	0.285±0.034	0.46±0.05	0.58±0.05
		0.30	0.35	0.112±0.028	0.199±0.024	0.241±0.027	0.38±0.04
		0.35	0.40	0.054±0.017	0.138±0.019	0.200±0.016	0.241±0.024
		0.40	0.45	0.038±0.014	0.096±0.014	0.175±0.015	0.186±0.021
		0.45	0.50	0.026±0.012	0.069±0.012	0.118±0.014	0.107±0.016
1.95	2.15	0.10	0.15	0.51±0.11	1.23±0.18	1.29±0.16	1.78±0.28
		0.15	0.20	0.44±0.06	0.76±0.07	0.98±0.06	1.31±0.09
		0.20	0.25	0.24±0.05	0.38±0.04	0.59±0.04	0.68±0.07
		0.25	0.30	0.080±0.030	0.198±0.030	0.34±0.05	0.383±0.034
		0.30	0.35	0.020±0.010	0.128±0.019	0.148±0.017	0.285±0.034
		0.35	0.40	0.019±0.010	0.114±0.020	0.124±0.014	0.147±0.023
		0.40	0.45	0.034±0.017	0.056±0.015	0.126±0.016	0.113±0.017
		0.45	0.50	0.037±0.018	0.032±0.010	0.091±0.014	0.111±0.017

B   Alternative analysis

The data taken in the 5 GeV/c beam have been analysed with an alternative analysis which is described in detail in Ref. [37]. While the unfolding procedure corrects for the efficiency, resolution smearing and a number of backgrounds in an integrated manner, this method makes sequential corrections for PID, energy-loss, efficiency and migration due to resolution smearing.

The alternative analysis proceeds with the following steps:

- The beam particle selection is identical to the one in the analysis described in this paper.

- The cut in the selection of the number of events accepted per spill is applied at 50 events reducing the sample[8].

- The basic track selection is identical. However, a stricter definition of the target volume is used. The cuts are applied at $|d'_0| < 8.5$ mm and -7.2 mm $< z'_0 \sin \theta < 12.8$ mm, corresponding to two standard deviations in the resolution. This selection reduces the tertiary background, but the efficiency correction is larger.

- A PID selection is applied based on the dE/dx of the particles and will be described below in more detail. The main difference is the method to determine the efficiency and backgrounds and the choice of the cut (which is more efficient but has a lower purity). This is one of the two main differences between the two methods.

- The correction for efficiency and absorption of secondary particles is applied bin–by–bin as multiplicative correction. This correction, although differently applied, is the same for both methods.

- The energy-loss correction is applied on a track–by–track basis, while in the method described in this paper it was part of the unfolding procedure.

- The resolution smearing correction is simpler; it does not consider the migration between angle bins (which is negligible), while it applies a multiplicative correction to account for the momentum smearing. It thus introduces a dependence on the assumed input spectra for this correction which contributes to the systematic error.

- The correction for π^0 background follows the same assumptions, but is quite different in implementation. The relative size of the subtraction is smaller owing to the stricter PID separation between pions and electrons (positrons).

- No subtraction for tertiary particles is applied. Although this is an approximation, the stricter target volume definition reduces this background to less than 2%.

The various corrections have been applied using the same simulation program as described in this paper. The differences in the analyses, both of principle and technical nature are large enough to provide a useful cross-check of the methods. Since the main difference between the analyses is given by the PID, this issue is described in somewhat more detail below.

The PID is based on a selection in dE/dx as a function of the momentum. The purity and the efficiency is evaluated studying the dE/dx spectra in the different momentum bins for each angular bin separately by fitting two Landau distributions to each spectrum. Particle separation between protons and pions can be achieved with a purity of about 99% up to 400 MeV/c (see Fig. 18). Above this value, efficiency and purity are lower as shown in Fig. 19. The two-component fits are used to determine these quantities as a function of the momentum in angular bins.

The electron contamination can be evaluated only for momenta less than 125 MeV/c. Above this value it is evaluated using a simulation. A similar assumption is made for the π^0 spectrum as in the analysis described in this paper. Using momenta below 125 MeV/c where the electrons can be identified, the

---

[8]This cut was decided consistently with other cuts on the impact point to define as clean as possible data samples.
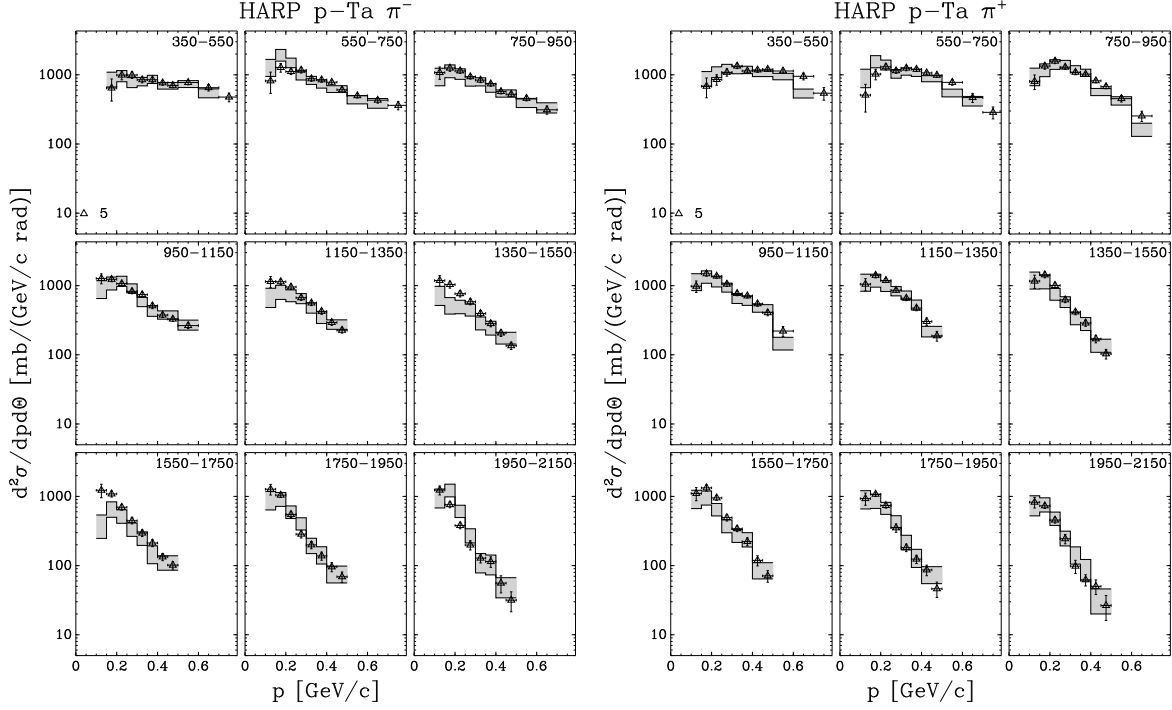
Figure 31: Comparison of the double-differential cross-sections measured for π^+ (right) and π^- (left) production in p–Ta interactions as a function of momentum displayed in different angular bins using the two analyses. The results of the alternative analysis are shown as shaded band and are available only for 5 GeV/c incident beam momentum. The width of the band represents an estimate of the uncorrelated error (one standard deviation) between the two methods. The results of the standard analysis described in this paper are represented by data points.

simulated data are normalized to obtain the same number of electrons and positrons as in the measured data.

The results of the alternative analysis are compatible with the results reported in Fig. 23 and 24 within the quoted systematic errors. The comparison is shown in Fig. 31. One observes good agreement between the two sets of spectra. Taking into account the large number of differences between the two approaches (event selection, track selection, energy-loss correction, particle identification, background subtraction) this constitutes an important cross-check of the correctness of the two analysis approaches.

References

[1] M.G. Catanesi *et al.*, HARP Collaboration, "Proposal to study hadron production for the neutrino factory and for the atmospheric neutrino flux", CERN-SPSC/99-35 (1999).

[2] G. Battistoni, Nucl. Phys. Proc. Suppl. **B100** (2001) 101.

[3] T. Stanev, Rapporteur's talk at the 26th Int. Cosmic Ray Conference (Salt Lake City, Utah, USA; eds. B.L. Dingus *et al.*, AIP Conf. Proceedings 516, (2000) 247).

[4] T.K. Gaisser, Nucl. Phys. Proc. Suppl. **B87** (2000) 145.

[5] R. Engel, T.K. Gaisser and T. Stanev, Phys. Lett. **B472** (2000) 113.

[6] M. Honda, Nucl. Phys. **B77** (1999) 140.

[7] M.H. Ahn *et al.*, K2K Collaboration, Phys. Rev. Lett. **90** (2003) 041801.

[8] M. H. Ahn *et al.*, K2K Collaboration, Phys. Rev. **D74** (2006) 072003, arXiv:hep-ex/0606032.

[9] E. Church *et al.*, BooNe Collaboration, "A proposal for an experiment to measure muon-neutrino → electron-neutrino oscillations and muon-neutrino disappearance at the Fermilab Booster: BooNE", FERMILAB-PROPOSAL-0898, (1997));
A. A. Aguilar-Arevalo *et al.*, BooNE Collaboration, arXiv:0704.1500, 2007.

[10] A. A. Aguilar-Arevalo *et al.*, SciBooNE Collaboration, "Bringing the SciBar detector to the Booster neutrino beam," FERMILAB-PROPOSAL-0954, (2006), arXiv:hep-ex/0601022.

[11] M. Apollonio *et al.*, "Oscillation Physics with a Neutrino Factory", CERN TH2002-208, arXiv:hep-ph/0210192;
A. Baldini *et al.*, BENE Steering Group, CERN-2006-005;
A. Blondel *et al.*, CERN-2004-002, ECFA/04/230.

[12] M.G. Catanesi *et al.*, HARP Collaboration, Nucl. Instrum. Meth. **A571** (2007) 527; **A571** (2007) 564.

[13] M. G. Catanesi *et al.*, HARP Collaboration, Nucl. Phys. **B732** (2006) 1, arXiv:hep-ex/0510039.

[14] M. G. Catanesi *et al.*, HARP Collaboration, Nucl. Instrum. and Methods **A572** (2007) 899.

[15] M. G. Catanesi *et al.*, HARP Collaboration, "Measurement of the production cross-section of positive pions in the collision of 8.9 GeV/c protons on beryllium", arXiv:hep-ex/0702024.

[16] M. Anfreville *et al.*, Nucl. Instrum. Methods **A481** (2002) 339.

[17] J. Altegoer *et al.*, NOMAD Collaboration, Nucl. Instrum. Methods **A404** (1998) 96.

[18] M. Baldo-Ceolin *et al.*, Nucl. Instrum. Meth. **A532** (2004) 548.

[19] S. Buontempo *et al.*, Nucl. Instrum. Meth. **A349** (1994) 70;
E. Di Capua *et al.*, Nucl. Instrum. Meth. **A378** (1996) 221.

[20] E. Radicioni, presented at NSS2004, IEEE Transaction on Nuclear Science, Vol 52, N 6 (2005) 2986.

[21] M. Bogomilov *et al.*, Nucl. Instrum. Methods **A508** (2003) 152;
G. Barr *et al.*, Nucl. Instrum. Methods **A533** (2004) 214.

[22] L. Durieu, A. Mueller and M. Martini, PAC-2001-TPAH142 *Presented at IEEE Particle Accelerator Conference (PAC2001), Chicago, Illinois, 18-22 Jun 2001*;
L. Durieu *et al.*, Proceedings of PAC'97, Vancouver, (1997);
L. Durieu, O. Fernando, CERN PS/PA Note 96-38.

[23] K. Pretzl *et al.*, Invited talk at the "International Symposium on Strangeness and Quark Matter", Crete, (1999) 230.

[24] J.W.E. Uiterwijk, J. Panman and B. Van de Vyver, Nucl. Instrum. Methods **A560** (2006) 317.

[25] J. Knobloch *et al.*, "Status of the Reconstruction Algorithms for ALEPH", ALEPH-Note 88-46.

[26] M.C. Morone, "Evaluation of Silicon sensors for the ATLAS Silicon Tracker, and TPC Reconstruction in the HARP Experiment", Ph.D. Thesis, University of Geneva, 2003.

[27] N.I. Chernov, G.A. Ososkov, Computer Physics Communications **33** (1984) 329.

[28] M. Bogomilov *et al.*, "Physics Performance of the Barrel RPC System of the HARP Experiment", IEEE Transaction on Nuclear Science **54** (2007) 342.

[29] S. Agostinelli *et al.*, GEANT4 Collaboration, Nucl. Instrum. Meth. **A506** (2003) 250.

[30] G. D'Agostini, Nucl. Instrum. Meth. **A362** (1995) 487.

[31] A. Grossheim, "Particle production yields induced by multi-GeV protons on nuclear targets", Ph.D. thesis, University of Dortmund, Germany, 2003, CERN-THESIS-2004-010.

[32] I. Chemakin *et al.*, E910 collaboration, Phys. Rev. **C65** (2002) 024904.

[33] D. Armutliiski *et al.*, "Hadron spectra in hadron–nucleus collisions" (in Russian), JINR-P1-91-191, 1991.

[34] K. Long, Nucl. Phys. B (Proc. Suppl.), **154** (2006) 111; ISS/2005/01, "An international scoping study of a Neutrino Factory and super-beam facility", http://www.hep.ph.ic.ac.uk/iss/issnotes/ISS_Doc1_v02_13-7-2005.pdf.

[35] R.C. Fernow and J. Gallardo, private communication; S.J. Brooks, private communication.

[36] S.J. Brooks and K.A Walaron, Nucl. Phys. B (Proc. Suppl.), **155** (2006) 295.

[37] S. Borghi, "Hadron production cross section measurement with the HARP large angle detectors", Ph.D. Thesis, N.3781, University of Geneva, Switzerland, 2006, CERN-THESIS-2007-034.